

## A Hybrid Bulk Algorithm to Predict Turbulent Fluxes over Dry and Wet Bare Soils

ANDREY A. GRACHEV,<sup>a,b</sup> CHRISTOPHER W. FAIRALL,<sup>a</sup> BYRON W. BLOMQUIST,<sup>a,b</sup> HARINDRA J. S. FERNANDO,<sup>c,d</sup>  
LAURA S. LEO,<sup>c,e</sup> SEBASTIÁN F. OTÁROLA-BUSTOS,<sup>c</sup> JAMES M. WILCZAK,<sup>a</sup> AND KATHERINE L. MCCAFFREY<sup>a,b</sup>

<sup>a</sup> NOAA/Physical Sciences Laboratory, Boulder, Colorado

<sup>b</sup> Cooperative Institute for Research in Environmental Sciences, University of Colorado, Boulder, Colorado

<sup>c</sup> Department of Civil and Environmental Engineering and Earth Sciences, University of Notre Dame, Notre Dame, Indiana

<sup>d</sup> Department of Aerospace and Mechanical Engineering, University of Notre Dame, Notre Dame, Indiana

<sup>e</sup> Department of Physics and Astronomy, Alma Mater Studiorum-University of Bologna, Bologna, Italy

(Manuscript received 11 October 2020, in final form 26 October 2021)

**ABSTRACT:** Measurements made in the Columbia River basin (Oregon) in an area of irregular terrain during the second Wind Forecast Improvement Project (WFIP2) field campaign are used to develop an optimized hybrid bulk algorithm to predict the surface turbulent fluxes from readily measured or modeled quantities over dry and wet bare or lightly vegetated soil surfaces. The hybrid (synthetic) algorithm combines (i) an aerodynamic method for turbulent flow, which is based on the transfer coefficients (drag coefficient and Stanton number), roughness lengths, and Monin–Obukhov similarity; and (ii) a modified Priestley–Taylor (P–T) algorithm with physically based ecophysiological constraints, which is essentially based on the surface energy budget (SEB) equation. Soil heat flux in the latter case was estimated from measurements of soil temperature and soil moisture. In the framework of the hybrid algorithm, bulk estimates of the momentum flux and the sensible heat flux are derived from a traditional aerodynamic approach, whereas the latent heat flux (or moisture flux) is evaluated from a modified P–T model. Direct measurements of the surface fluxes (turbulent and radiative) and other ancillary atmospheric/soil parameters made during WFIP2 for different soil conditions (dry and wet) are used to optimize and tune the hybrid bulk algorithm. The bulk flux estimates are validated against the measured eddy-covariance fluxes. We also discuss the SEB closure over dry and wet surfaces at various time scales based on the modeled and measured fluxes. Although this bulk flux algorithm is optimized for the data collected during the WFIP2, a hybrid approach can be used for similar flux-tower sites and field campaigns.

**KEYWORDS:** Atmosphere-land interaction; Fluxes; Heat budgets/fluxes; Water vapor; Parameterization

### 1. Introduction

Determination of momentum, heat, and mass exchange between the atmosphere and the underlying surface is a central problem of atmospheric boundary layer (ABL) research. Understanding and proper parameterization of the surface turbulent fluxes (e.g., flux–profile relationships) is of obvious relevance for the modeling of the coupled atmosphere–land/ocean system, including climate modeling, weather forecasting, environmental impact studies, and many other applications. It should be noted that with the exception of direct numerical simulations the surface fluxes are always subgrid-scale processes that cannot be explicitly resolved and must be parameterized, regardless of how high the resolution of a numerical model is. At present, in almost all numerical models, from local and mesoscale to global models (i.e., in weather prediction and climate models), turbulence fluxes are parameterized using Monin–Obukhov similarity theory (MOST) or/and a bulk flux algorithm.

A direct application of the turbulent energy fluxes is the net surface energy budget (SEB). An accurate determination of energy balance closure and all components of the SEB at the air–surface interface are required in a wide variety of applications including atmosphere–land/snow simulations and validation of the surface fluxes predicted by numerical models over representative spatial and temporal scales.

Recently, progress has been made in our understanding of the turbulent mixing and development of bulk schemes over, more or less, horizontally homogeneous surfaces such as the open ocean (e.g., the COARE bulk flux algorithm by Fairall et al. 1996, 2003) and snow-covered sea ice (e.g., the SHEBA bulk turbulent flux algorithm by Andreas et al. 2010a,b). Because of the complexity of vegetated and bare (or lightly vegetated) surfaces, an equivalent progress in development of simplified bulk algorithms over land is not as straightforward as in the case of the over water or snow/ice but appears feasible in this case. In this study, surface fluxes (turbulent and radiative) and other ancillary atmospheric and soil data collected in the Columbia River Gorge area near Wasco, Oregon, during 2016–17 within the second Wind Forecast Improvement Project (WFIP2), are used to develop a hybrid bulk flux algorithm utilizing the available WFIP2 experimental data.

The novelty of the present study is to develop a hybrid or synthetic (in the sense of “combination”) bulk approach to predict the surface turbulent fluxes from tower-based measurements. Traditional bulk flux schemes (e.g., the

---

Grachev’s current affiliation: Boundary Layer Research Team/ Atmospheric Dynamics and Analytics Branch, DEVCOM Army Research Laboratory, WSMR, New Mexico.

McCaffrey’s current affiliation: S & P Global Commodity Insights, Boulder, Colorado.

---

*Corresponding author:* Andrey A. Grachev, andrey.grachev@colorado.edu

DOI: 10.1175/JAMC-D-20-0232.1

© 2022 American Meteorological Society. For information regarding reuse of this content and general copyright information, consult the [AMS Copyright Policy \(www.ametsoc.org/PUBSReuseLicenses\)](#).

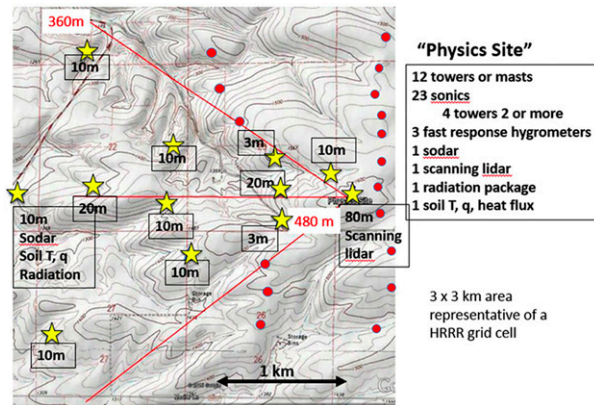


FIG. 1. Elevation map showing the Physics site with terrain contours. Red dots are wind turbine locations; yellow stars are instrumented towers (3–20 m tall). The leftmost yellow star in the center indicates location of the 10-m PS01 flux tower. Oblique red lines indicate the angle of flow unobstructed by wind turbines for the prevailing westerly wind direction.

COARE and SHEBA algorithms) derive all three turbulent fluxes (momentum, sensible, and latent heat) in the same way. The hybrid bulk flux algorithm developed in this study derives the turbulent fluxes of momentum and sensible heat from the traditional aerodynamic method for the turbulent flow (similar to the COARE and SHEBA algorithms), whereas the latent heat flux is estimated from a method that is essentially based on the conservation of energy principle (i.e., the surface energy balance at the surface–atmosphere interface). Although our bulk flux algorithm is based on the WFIP2 data, the hybrid approach developed here can be applied to similar tower-based measurements over land to predict the turbulent fluxes.

The paper is organized as follows: [Section 2](#) contains information about the observation site, instrumentation, and dataset collection. [Section 3](#) provides a formal background for measuring and modeling surface fluxes including the SEB closure problem and traditional bulk flux approach. In [section 4](#), we develop and verify a hybrid bulk flux algorithm for computing surface fluxes from readily measured or modeled during WFIP2 bulk quantities. The conclusions are summarized in [section 5](#). Some material presented in the current study, for example, associated with the description of the observation site, instrumentation, and data ([section 2](#)), is partially repeated here from [Grachev et al. \(2020\)](#). Both studies use the same WFIP2 dataset but for different problems.

## 2. Observation site, instrumentation, and data

This study analyzes and discusses the data collected during a 10-month-long portion of the WFIP2 field campaign (for details, see [Bianco et al. 2019](#); [Olson et al. 2019](#); [Shaw et al. 2019](#); [Wilczak et al. 2019](#)). [Grachev et al. \(2020\)](#) described the measurement site, instruments, various observations, data processing etc. in detail. Here we provide some relevant information about the turbulent and profile measurements in the near-surface atmosphere and soil layer during the WFIP2 project.

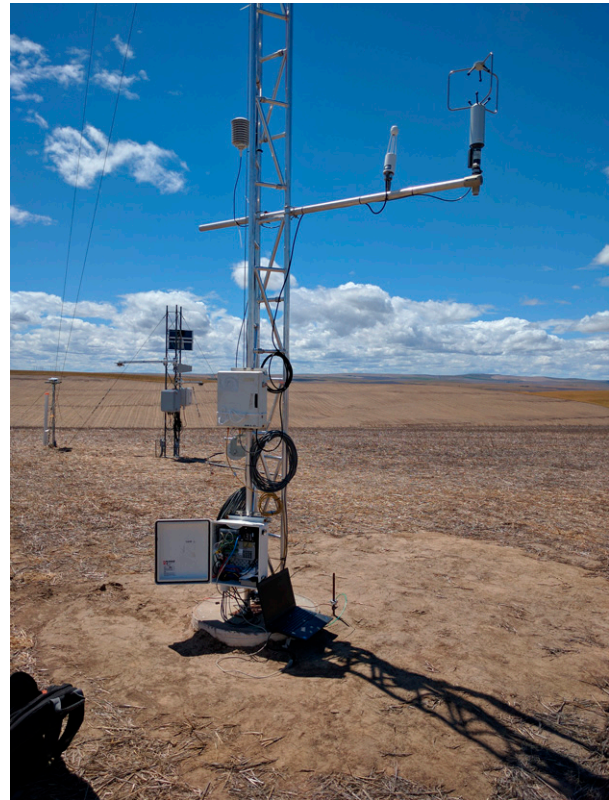


FIG. 2. View of the 10-m PS01 flux tower showing the lower (3-m) measurement level during summer conditions (23 Jun 2016). The two radiation masts for measurements of the downwelling and upwelling radiation are located right behind the flux tower in this photo.

The WFIP2 field campaign took place in an area of irregular terrain along the Columbia River Gorge in eastern Oregon and Washington states ([Fig. 1](#)). Here we use measurements of 30-min averaged surface fluxes and basic meteorological/soil parameters from the Physics Site 1 tower (PS01) located near Wasco. The PS01 study area encompasses relatively flat plain (e.g., [Fig. 2](#)) and a ridge (e.g., [Grachev et al. 2020](#), their Fig. 2) sited in irregular terrain of moderate complexity. The ridge is aligned approximately in a west–east direction. The instruments at the PS01 site ([Figs. 1](#) and [2](#)) were deployed in an area similar to a high-resolution model grid cell for observing subgrid-scale turbulent processes ([Shaw et al. 2019](#)). According to [Grachev et al. \(2020](#), their Fig. 3b), prevailing winds observed at PS01 site have a bimodal distribution with the two dominant wind directions  $\approx 180^\circ$  apart (easterly and westerly winds). These predominant winds generally blow parallel to the ridge and not frequent southerly wind directions are generally associated with light winds. Turbulent fluxes and other ancillary atmospheric data at the PS01 site were measured continuously on a 10-m meteorological tower at 3- and 10-m levels ([Fig. 2](#)) from 24 June 2016 to 1 May 2017, yeardays (YD) 176–487 with respect to 1 January 2016 UTC. Each level was instrumented with identical fast-response

three-axis sonic anemometers sampling wind velocity and sonic temperature at 20 Hz (R.M. Young Model 81000) and Rotronics HC2S3 temperature and relative humidity probes ( $T/RH$ , sampling frequency = 1 Hz). The HC2S3 probes were housed in ventilated radiation shields. A fast-response (20 Hz) infrared gas analyzer (LI-7500) was collocated at 3-m height with the lower sonic anemometer. The mean wind speed and wind direction were derived from the sonic anemometers using the ordinary planar-fit method rotation of the coordinate system proposed by Wilczak et al. (2001). Several data-quality indicators based on objective and subjective methods have been applied to the original flux data to remove spurious or low-quality records (e.g., Bariteau et al. 2010; Grachev et al. 2011, 2015; Blomquist et al. 2014, and references therein). Specifically, turbulent data have been edited for unfavorable relative wind direction for which the tower was upwind of the sonic anemometers, nonstationarity, minimum or/and maximum thresholds for the turbulent statistics, etc. In particular, sonic anemometer data based on the planar-fit procedure were flagged as bad if the mean vertical velocity component differed by more than  $0.2 \text{ m s}^{-1}$  from the plane. For example, after data-quality control screening, the number of data points for sensible heat  $H_S$  and latent heat  $H_L$  fluxes measured at the 3-m level during the entire WFIP2 field campaign decreased to  $\approx 90.2\%$  and  $\approx 79.6\%$  of the original amount, respectively.

Measurements of soil temperature and moisture were made at five levels located nominally at 5-, 10-, 20-, 50-, and 100-cm depths below the ground surface approximately 5 m from the flux tower. Note that no direct measurements of surface soil heat flux with a heat flux plate were performed at this site. The soils at the WFIP2 Physics Site PS01 are primarily well-drained silt (73%), with minor components of sand (14%), and clay (13%) and average 152 cm in depth before reaching harder rock. In general, the underlying surface at the PS01 site can be described as bare and/or short vegetation surface (cf. Cuxart and Boone 2020, their Fig. 1). The downwelling and upwelling shortwave and infrared radiation was measured from two radiation masts located near the flux tower by Eppley pyranometers and pyrgeometers, respectively (Fig. 2). The “slow”-response data used in this study ( $T/RH$ , solar radiation, soil temperature and moisture) are based on 1-Hz raw measurements that were averaged over 1-min time intervals.

The time series of half-hour averaged surface fluxes and basic meteorological variables to describe weather and soil conditions, surface fluxes, and other relevant variables as observed during the entire WFIP2 field campaign for the period 24 June 2016 to 1 May 2017 (YD 176–487 with respect to 1 January 2016 UTC) can be found in Grachev et al. (2020, Figs. 3–6). Similar to Grachev et al. (2020, section 4.1), in this study we sort the data into dry and wet categories (the soil moisture content below is the volumetric soil moisture):

- (i) *Dry bare (or lightly vegetated) soil surfaces*, if the soil temperature at 5-cm depth is  $>1^\circ\text{C}$  and the volumetric soil moisture at 5-cm depth is  $\leq 0.07$ .
- (ii) *Wet bare (or lightly vegetated) soil surfaces*, if the soil temperature at 5-cm depth is  $>1^\circ\text{C}$  and the volumetric soil moisture at 5-cm depth is  $>0.07$ .

According to our data, dry and wet surfaces for this location and for the considered time intervals are generally associated with the volumetric soil moisture at 5-cm depth under 0.05 and above 0.15, respectively (Grachev et al. 2020, Fig. 4b). Range between 0.05 and 0.15 can be considered as a transition interval. However, our data show that the surface soil moisture increases rapidly during approximately two days around YD 291 with the onset of the rainy season (Grachev et al. 2020, Figs. 4b–d). Thus, transition from the dry soil case to the wet-soil case has occurred within a fairly short period of time and, for this reason, the choice of any value from the transition range as a threshold (e.g., 0.07) has little or no effect on the final results.

The original 10-month-long in situ data often contain gaps (Grachev et al. 2020, Figs. 3–6). To calibrate and verify the bulk flux algorithm over different soil conditions, we use in this study a 30-day-long uninterrupted time series of relatively good data separately for dry and wet soil conditions (WFIP2 “golden files”) described by Grachev et al. (2020, section 4.4). Data collected during yeardays 240–270 (27 August–26 September 2016) provide an illustrative example of surface meteorology and surface fluxes observed at the WFIP2 Physics site PS01 for dry soils. Similarly, the 30-day-long time period from 25 March to 24 April 2017 (YD 450–480 with respect to 1 January 2016) was selected to analyze data over wet soil surfaces.

Figures 3–6 show continuous monthly (30-day-long) records of the surface fluxes and surface meteorology for dry and wet soils, respectively. The data presented in Figs. 3–6 and some other ancillary information for these time periods are used in this study to test the bulk algorithm. Additionally, the time series of the SEB components (the net radiation, the sum of the sensible and latent heat fluxes, the SEB residual) over dry and wet soils for the same time periods as in Figs. 3–6 in the current study can be found in Grachev et al. (2020, Figs. 10 and 11). Thereby, we use a subset of the data analyzed in our previous study (Grachev et al. 2020), though of a higher quality.

As expected, variations of the air temperature, topsoil temperature, and the turbulent energy fluxes  $H_S$  and  $H_L$  have a pronounced diurnal cycle (Figs. 3–6). We note different behavior of  $H_S$  and  $H_L$  for different soil conditions. According to Figs. 4a and 6a, values of the half-hourly  $H_S$  at local noon are generally larger for drier than for wetter soils, whereas the situation with  $H_L$  is obviously opposite. The turbulent flux of the latent heat shown in Fig. 4b is small over dry soil surfaces indicating that evaporation is negligible for drier than for wetter soils (cf. Fig. 6b). Furthermore, diurnal variations of  $H_L$  are much less evident in the case of dry soil conditions (Fig. 4b). Note also that in general the soil moisture increases with increasing depth for dry soils (Fig. 3d) and vice versa for wet soils (Fig. 5d).

Other details regarding the observation site, the instrumentation, and the data can be found in Grachev et al. (2020).



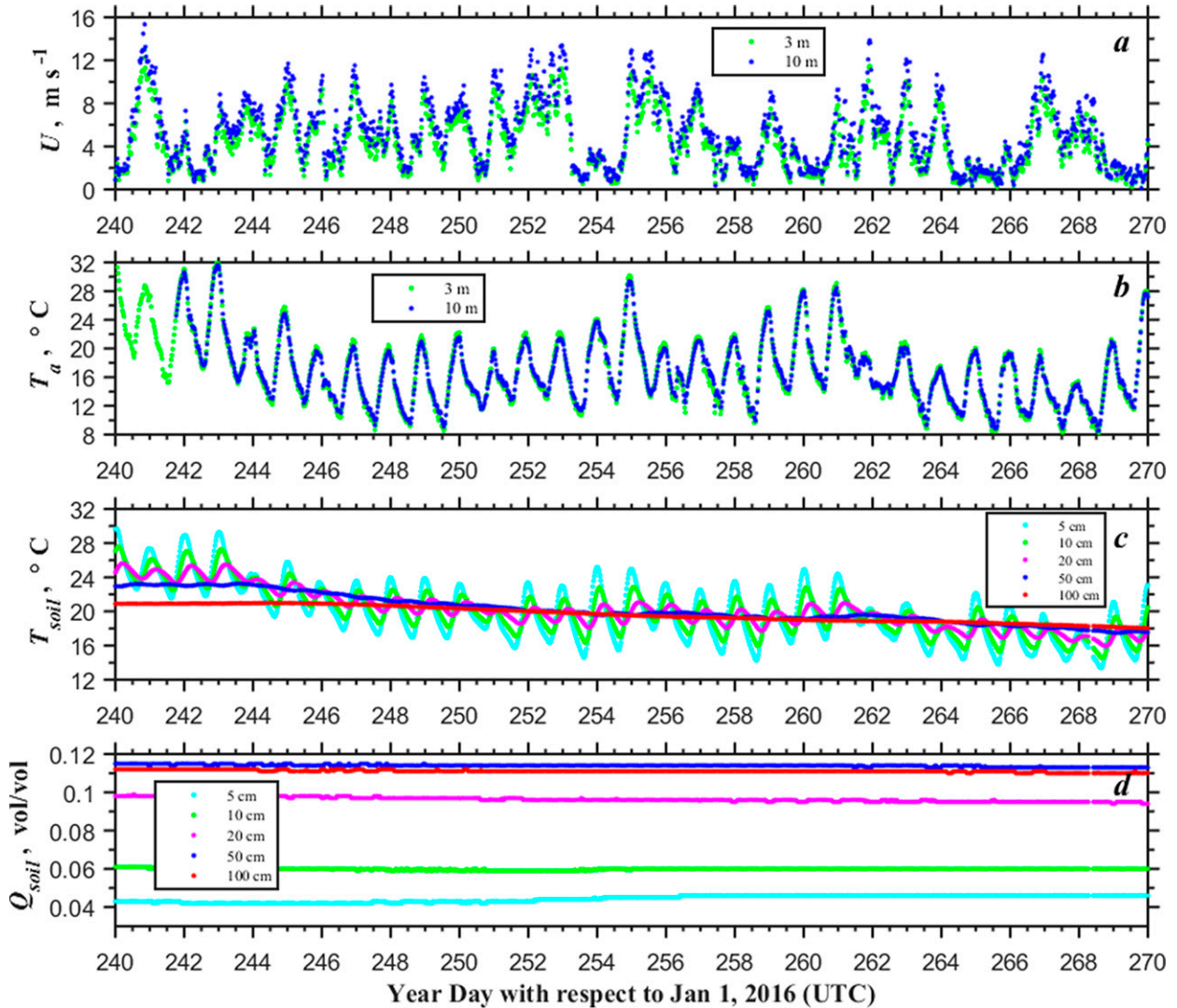


FIG. 3. A 1-month (30 day) time series of (a) wind speed, (b) air temperature, (c) soil temperature, and (d) volumetric soil moisture observed at the WFIP2 Physics site PS01 during YD 240–270 (27 Aug–26 Sep 2016). The data are based on half-hour averaging.

### 3. Measuring and modeling surface fluxes

The turbulent fluxes of momentum  $\tau$  (or magnitude of the wind stress), sensible heat  $H_S$ , and latent heat  $H_L$  can be estimated by the eddy-correlation method according to

$$\tau = \rho u_*^2, \quad (1)$$

$$H_S = c_p \rho \overline{w'\theta'} = -c_p \rho u_* \theta_*, \quad (2)$$

$$H_L = \mathcal{L}_e \rho \overline{w'q'} = -\mathcal{L}_e \rho u_* q_*, \quad (3)$$

where  $\rho$  is the mean air density,  $\theta$  is the air potential temperature,  $q$  is the air specific humidity,  $c_p$  is the specific heat capacity of air at constant pressure,  $\mathcal{L}_e$  is the latent heat of evaporation of water,  $u_*^2 = \sqrt{(\overline{w'u'})^2 + (\overline{w'v'})^2}$  ( $u_*$  is the

friction velocity),  $\theta_* = -\overline{w'\theta'}/u_*$  and  $q_* = -\overline{w'q'}/u_*$  are the temperature and the specific humidity scales, respectively. Here  $w$  is the vertical velocity component, the prime ( $'$ ) denotes fluctuations about the mean value, and an overbar is an averaging operator (half an hour in this study). Note that in Eq. (1),  $\tau$  is based on the both longitudinal (or downstream),  $\tau_x = -\rho \overline{w'u'}$ , and the lateral (or crosswind),  $\tau_y = -\rho \overline{w'v'}$ , components of wind stress (see Grachev et al. 2011 for discussion).

#### a. SEB closure

Knowledge of the surface energy fluxes (2) and (3) is considered fundamental to the SEB. Typically, the SEB equation accounts for energy inputs and outputs at the infinitesimal interface between atmosphere and land and it is assumed that the energy budget must balance; that is, the SEB equation is a

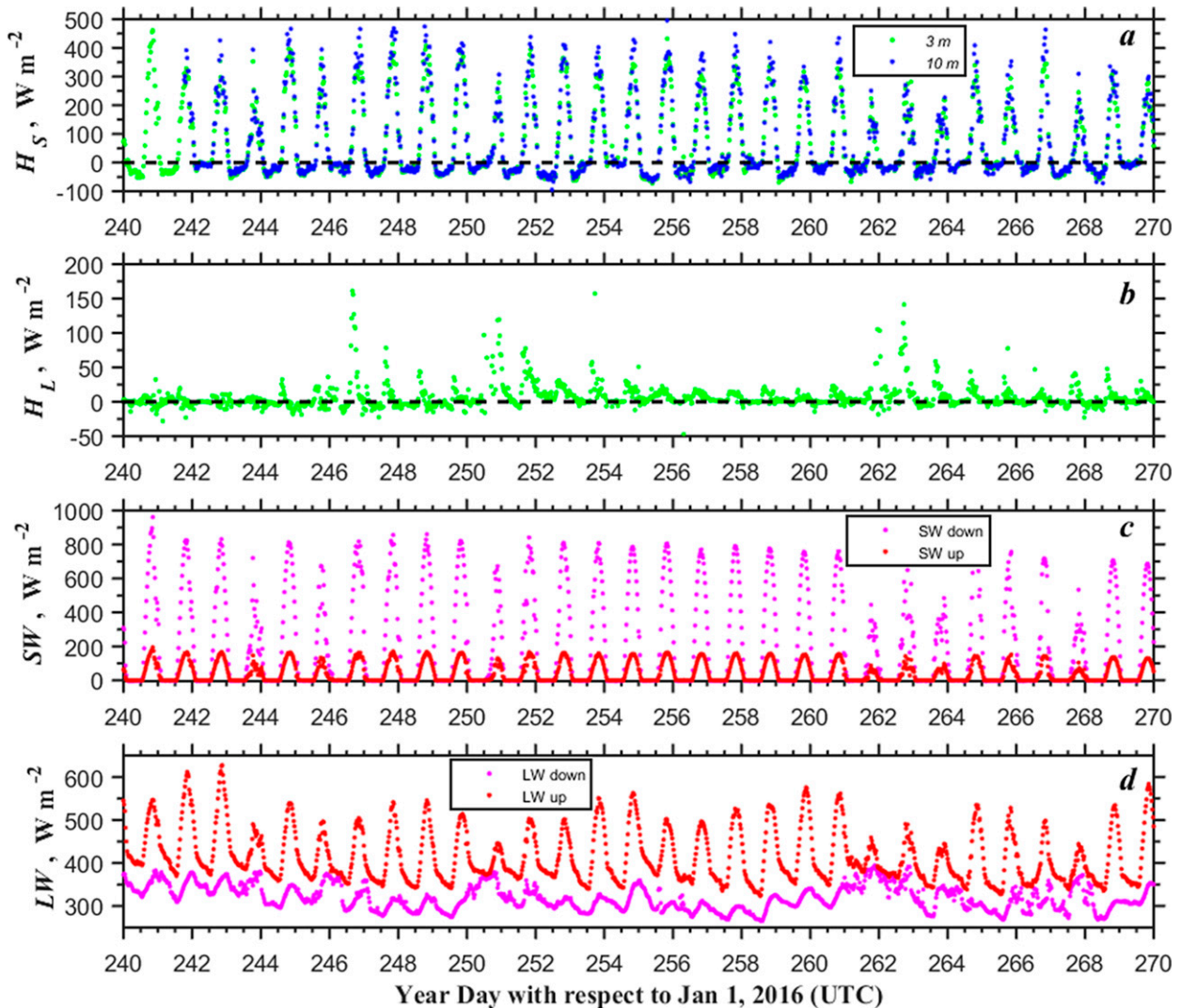


FIG. 4. A 1-month (30 day) time series of (a) sensible heat flux measured at 3 and 10 m, (b) latent heat (water vapor) flux measured at 3 m, (c) shortwave (SW) downwelling and upwelling radiation, and (d) longwave (LW) downwelling and upwelling radiation observed at the WFIP2 Physics site PS01 during YD 240–270 (27 Aug–26 Sep 2016). The data are based on half-hour averaging.

balance equation. Thus, the classical formulation of the SEB equation is

$$H_S + H_L + G = R_{\text{net}}, \quad (4)$$

where  $G$  is the soil heat flux,  $R_{\text{net}}$  is the net radiation defined as the balance between downwelling and upwelling SW and LW radiation:

$$R_{\text{net}} = \text{SW}_{\text{down}} - \text{SW}_{\text{up}} + \text{LW}_{\text{down}} - \text{LW}_{\text{up}}. \quad (5)$$

Note that unlike the momentum flux  $\tau$  (1), the turbulent energy fluxes  $H_S$  and  $H_L$  are highly correlated with the net radiation  $R_{\text{net}}$  due to the SEB equation (e.g., Grachev et al. 2020, Fig. 8), providing an objective approach for a land surface model or numerical models of the climate system to estimate missing terms (e.g.,  $H_S$  or  $H_L$ ) as the residual of the

others based on (4), which is traditionally considered to have to be closed (e.g., Cuxart et al. 2015, and references therein). A similar approach is used in soil–vegetation–atmosphere transfer schemes where the surface energy fluxes are estimated from thermal infrared data (i.e., radiometric surface temperature) and SEB, Eq. (4) (e.g., Priestley and Taylor 1972; Su 2002; Kustas et al. 1993, 2004; Yao et al. 2015, and references therein). In the next section, we develop a method of estimating  $H_L$  on the basis of the surface energy balance.

In practice, the soil heat flux  $G$  in (4) can be measured at some reference depth  $z$  below the ground surface by a heat flux plate or estimated from soil temperature profile measurements using Fourier's law of heat conduction (gradient method):

$$G(z) = -\lambda \frac{\partial T_S}{\partial z}, \quad (6)$$

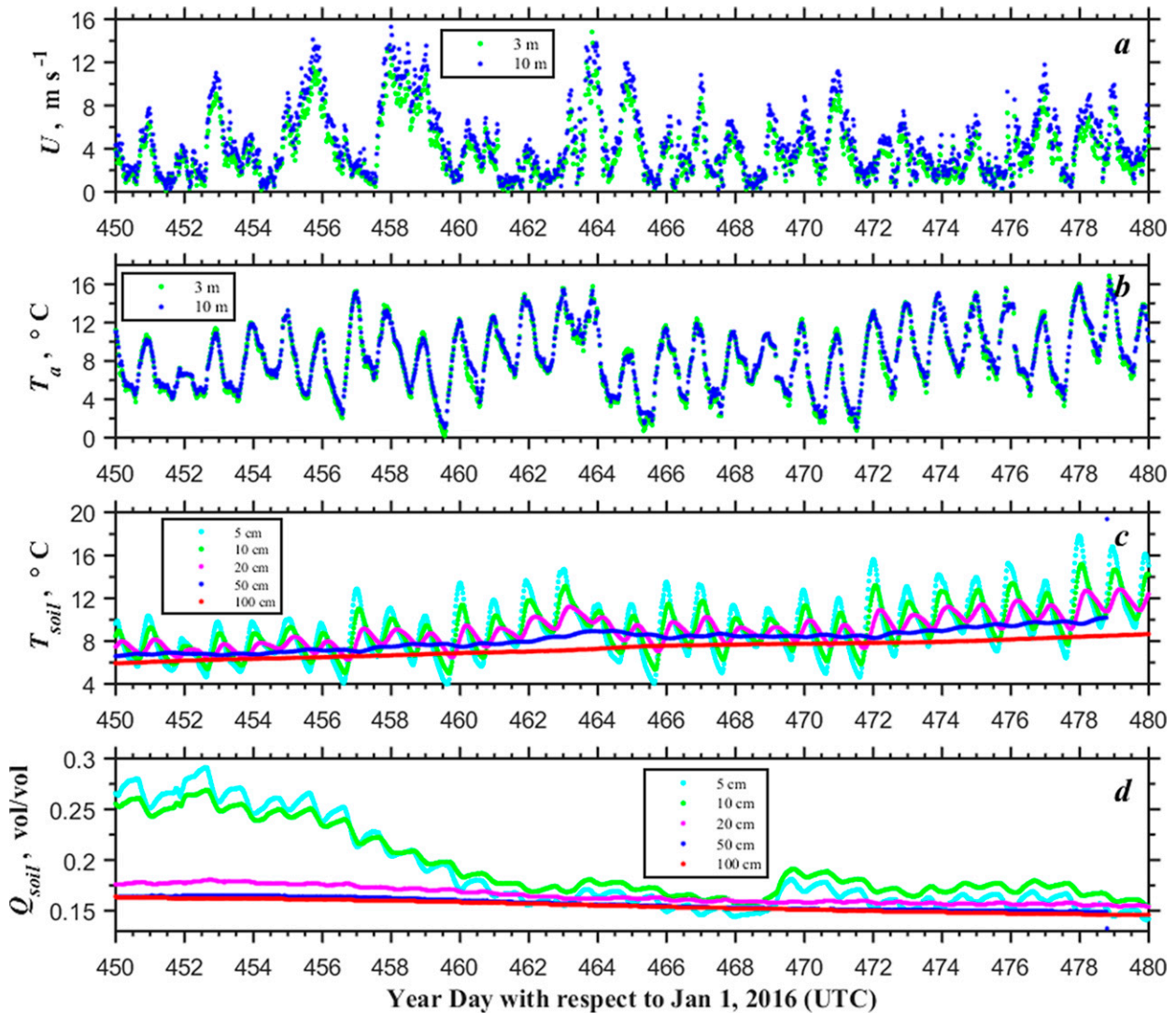


FIG. 5. As in Fig. 3, but for wet soils observed at the WFIP2 Physics site PS01 during YD 450–480 (25 Mar–24 Apr 2017). The data are based on half-hour averaging.

where  $\lambda$  is the thermal conductivity of the soil and  $\partial T_S/\partial z$  is the vertical temperature gradient of the soil temperature  $T_S$ . Traditionally,  $\partial T_S/\partial z$  in the soil layer  $\Delta z$  is replaced by  $\Delta T_S/\Delta z$  and Eq. (6) reduces to  $G(z) \approx -\lambda \Delta T_S/\Delta z$ .

Surface energy balance closure in (4) is a formulation of the conservation of energy principle at the interface and Eq. (4) assumes an ideal case, when all the fluxes are measured at the infinitesimal interface between the atmosphere and the soil and it is a statement of how the net radiation [Eq. (5)] is balanced by turbulent sensible [Eq. (2)], latent [Eq. (3)], and soil [Eq. (6)] heat fluxes in the absence of other energy sources and sinks. However, many studies reported that the surface energy balance [Eq. (4)] is difficult to close at temporal scales less than several hours (e.g., Wilson et al. 2002; Foken et al. 2006; Mauder et al. 2007, 2020; Oncley et al. 2007; Cava et al. 2008; Foken 2008; Jacobs et al. 2008; Higgins 2012; Leuning

et al. 2012; Stoy et al. 2013; Cuxart et al. 2015; Majozi et al. 2017; Gao et al. 2017a; Grachev et al. 2020, and references therein). Direct measurements of energy budget at these time scales (in particular, at half-hourly and hourly averaged time scales) showed that in most cases the sum of the turbulent fluxes of sensible and latent heat plus the ground heat flux systematically is lower than the net radiation by around 20%–30% during daytime and generally is higher than the net radiation at night.

Because the fluxes cannot be measured at the surface and the energy balance often cannot be closed based on experimental data, the SEB in Eq. (4) is reformulated for a control volume instead of at the interface of the two media (e.g., Foken et al. 2006; Mauder et al. 2020):

$$H_S + H_L + G + \text{Res} = R_{\text{net}}, \quad (7)$$



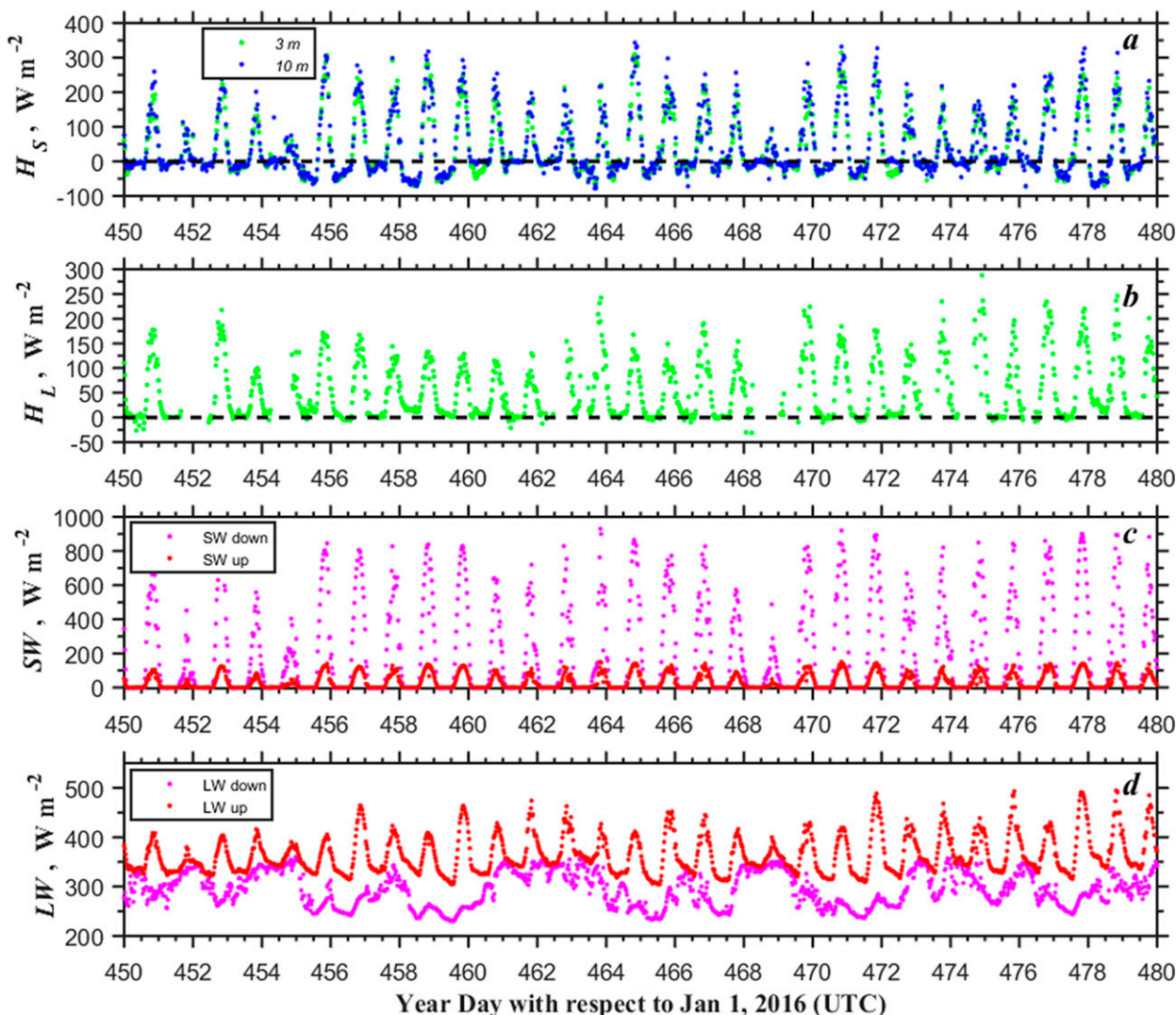


FIG. 6. As in Fig. 4, but for wet soils observed at the WFIP2 Physics site PS01 during YD 450–480 (25 Mar–24 Apr 2017). The data are based on half-hour averaging.

where “Res” is a residual term. Note, that Eq. (7) implies now a two-layer (atmosphere and soil) column of finite thickness (e.g., Foken 2008, his Fig. 1) where the turbulent fluxes in (1)–(3) and the net radiation in (5) are measured at the upper boundary plane whereas the soil flux is measured at the lower boundary plane of the total layer, respectively. In the general case, Res can be partitioned as the sum of an additional transport (vertical and horizontal) term through all boundary planes, a total storage term in the two-layer column (air and soil), and all other reasons unaccounted in (4), which can be also responsible for the SEB imbalance. The storage term in turn can be partitioned as a sum of storage of energy in the air column due to radiative and/or sensible heat flux divergence (the air enthalpy change), ground heat storage above a near-surface reference point, radiation consumed in photosynthesis (the photosynthesis flux), canopy heat storage in biomass (the rate change in enthalpy of the vegetation), as

well as all other storage terms (e.g., Meyers and Hollinger 2004, Jacobs et al. 2008; Leuning et al. 2012, Masseroni et al. 2014).

A variety of factors (except of  $H_S$ ,  $H_L$ ,  $R_{\text{net}}$ , and  $G$ ) may be responsible for the lack of SEB closure. For example, failure to close the energy balance may be associated with storage of energy in the air column due to radiative and/or sensible heat flux divergence (the air enthalpy change), the ground heat storage above a heat flux plate measurement level, the radiation consumed in photosynthesis (the photosynthesis flux), the canopy heat storage in biomass (the rate change in enthalpy of the vegetation), and other storage terms, for example, the atmospheric moisture change and the canopy dew water enthalpy change (e.g., Mauder et al. 2020). In addition, another complexity of the SEB closure is associated with nonstationarity (diurnal variations), even during a half-hour averaging period (e.g., Garratt 1992). The diurnal cycle of solar radiation

modulates a sinusoidal variation in the ground surface heat flux and diurnal thermal waves in the top soil layer. The impact of the hysteresis effect in diurnal cycles and the effect of the wave phase difference between different atmospheric and/or soil variables on the SEB closure are discussed in number of studies (e.g., Gao et al. 2017a, and references therein). It is generally accepted that the underestimation of the sensible and latent heat fluxes is associated with large-scale nonturbulent transport mechanisms at low-frequencies such as boundary layer scale eddies under convective conditions, mesoscale and submesoscale transport, secondary circulations etc. (Foken 2008; Mauder et al. 2020). According to Grachev et al. (2020), extending the averaging time consistently from half-hourly to daily, weekly, monthly, seasonal, and subannual time scales (311-day averaging for the entire WFIP2 field campaign) significantly reduces the SEB imbalance on average. Increasing the averaging time to daily and longer time intervals substantially reduces averaged ground heat flux and storage terms, because energy locally entering the soil, air column, and vegetation in the morning and during the first half of the day is released in the afternoon, evening, and night.

#### b. Traditional bulk turbulent flux algorithm

In almost all numerical weather prediction and climate models the turbulent fluxes of momentum  $\tau$ , sensible heat  $H_S$ , and latent heat  $H_L$ , Eqs. (1)–(3), are estimated using MOST or/and a bulk flux algorithm. In this study, we will use a bulk formulation, which is in part based on the COARE bulk flux algorithm derived for open ocean (Fairall et al. 1996, 2003), and the SHEBA bulk flux algorithm developed for sea ice conditions (Andreas et al. 2010a,b). We will use observations from the WFIP2 Physics Site PS01 to evaluate bulk representations of the turbulent and ground fluxes, including the turbulent surface stress  $\tau$ , because  $u_*$  is required for surface layer similarity theory that forms the basis of bulk turbulent flux algorithms.

The turbulent fluxes are parameterized by bulk aerodynamic relationships, which relate fluxes to mean properties of the flow through the height-dependent transfer coefficients:  $C_D$  (the drag coefficient),  $C_H$  (the Stanton number), and  $C_E$  (the Dalton number):

$$\tau = C_D \rho S U, \quad (8)$$

$$H_S = C_H c_p \rho S \Delta \theta, \quad (9)$$

$$H_L = C_E \mathcal{L}_e \rho S \Delta q, \quad (10)$$

Here,  $\Delta \theta = (\theta_0 - \theta_a)$  and  $\Delta q = (q_0 - q_a)$ , where subscripts 0 and  $a$  for the potential temperature  $\theta$  and the air specific humidity  $q$  denote their surface (“skin,”  $z = 0$ ) and atmospheric reference height values, respectively. It is often assumed that the water vapor and other scalars (e.g., carbon dioxide and methane) are transported similarly to the temperature, that is, with the same efficiency (the Lewis analogy) and, therefore,  $C_H = C_E$ . Note, that accurate estimation of the transfer coefficients in (8)–(10) is a crucial problem of

air–sea–land interaction. The transfer coefficients depend on stratification (atmospheric stability) and roughness lengths (e.g., Fairall et al. 1996, 2003). Scalar-averaged wind speed  $S$  in (8)–(10) is defined and discussed in the appendix.

#### 4. Hybrid bulk algorithm and analysis of the WFIP2 data

Following the discussion in the section 3 and in the appendix, turbulent fluxes are computed from (8)–(10) and (A4) via an iteration because the transfer coefficients depend on the MOST stability parameter  $z/L$ , which is computed from the fluxes (see Fairall et al. 1996, 2003). The forms of (8)–(10) apply well to reasonably statistically homogeneous surfaces where an interfacial value of  $q_0$  can be unambiguously established—oceans, lakes, ice, snow-covered surfaces, or water-saturated soils where we can assume  $q_0$  is the water saturation value at temperature  $\theta_0$ . For dry and wet bare soils or simple ground-hugging plant canopies, Eqs. (8) and (9) still work but in general case in Eq. (10) does not apply because the surface is not near saturation. Kondo et al. (1990) show that application of Eq. (10) for parameterization of evaporation from bare soil surfaces requires coupling with a special model of molecular diffusion of water vapor in the surface soil pore with the vapor being carried from the interior of the soil pore to the land surface.

Various techniques to represent  $H_L$  over land surfaces have been reported in the literature (see Garratt 1992; Foken 2017 for background). The most widely used model is the physically based Penman–Monteith (P-M) model (Penman 1948; Monteith 1965; De Bruin and Holtslag 1982), which combines the SEB and aerodynamic transport equations, assuming that surface meteorological observations are available. An alternative approach, the Priestley–Taylor (P-T) algorithm, is relatively simple and can be considered as a simplified P-M method that avoids parameterizations of aerodynamic and surface resistance without decreasing the accuracy of the  $H_L$  estimates (Priestley and Taylor 1972). Both the P-M and P-T methods have been shown to give relatively low biases, particularly in comparison with the relatively poor accuracy of other methods (Fisher et al. 2008).

The SEB Eq. (4), which is assumed to be closed, is the starting point in the P-T model. The Bowen-ratio method and the Clausius–Clapeyron equation are also used in the derivation of the P-T relationship (e.g., Foken 2017). Although the original P-T method (Priestley and Taylor 1972) was developed for saturated surfaces, it has been widely extended to unsaturated surfaces. Different modified P-T models are based on parameters that relate the saturated and unsaturated surfaces and parameterization of the atmospheric and resistance variables (“constraint functions”). Further discussion regarding various modifications of the P-T model can be found in De Bruin (1983), Fisher et al. (2008), Venturini et al. (2011), Yao et al. (2013, 2014, 2015), and Hao et al. (2019) among others. The P-T model stands for its simplicity and low data requirements (e.g., where ground observations of aerodynamic and surface resistance is not available) and for this reason the P-T approach is widely used as a satellite-based  $H_L$  algorithm and remote sensing technology that enables



TABLE 1. The hybrid bulk flux algorithm parameters and equations.

Flux variables	Equations	Coefficients	Input variables
$\tau, H_S$	(A1), (A2), (A7)	$C_D, C_H$	$U, \theta_0, \theta_a, q_a$
$H_L$	(8), (9)	$\alpha, k_i$	$R_{\text{net}}, G$
$G$	(12)	$\lambda, \rho_s, c_{pS}$	$\theta_0, T_{S5}$

estimation of the terrestrial  $H_L$  at regional or global scales (e.g., Fisher et al. 2008; Li et al. 2009; Venturini et al. 2011; Yao et al. 2013, 2014, 2015). Further discussion, the state of the art, and perspectives on determining evapotranspiration by various methods (including MOST, P-M, and P-T approaches) can be found in a review paper by Cuxart and Boone (2020).

In this study, we follow a modified P-T model by Yao et al. (2015) to estimate  $H_L$  over dry and wet bare soils during the WFIP2 field campaign. The approach by Yao et al. (2015)

combines the P-T method, which avoids the uncertainty associated with the Dalton transfer coefficient and an effective surface relative humidity in (10) with physically based ecophysiological constraints. According to a modified P-T model by Yao et al. (2015), the latent heat flux  $H_L$  can be expressed as

$$H_L = \alpha \frac{\Delta_s}{\Delta_s + \gamma} f(e)(R_{\text{net}} - G), \quad (11)$$

where  $\Delta_s$  is the temperature derivative from the saturated vapor pressure relationship (see Priestley and Taylor 1972 for detail),  $\gamma$  the psychrometric constant,  $f(e)$  the sum of the weighted ecophysiological constraints, and  $\alpha$  the P-T parameter. According to Priestley and Taylor (1972), the empirical parameter  $\alpha$  in (11) equal to 1.26 on average for saturated surfaces. In general, the P-T parameter  $\alpha$  varies with soil moisture, the canopy resistance, thermal stratification, etc. and has a diurnal cycle (e.g., De Bruin 1983; Lhomme 1997; Pereira

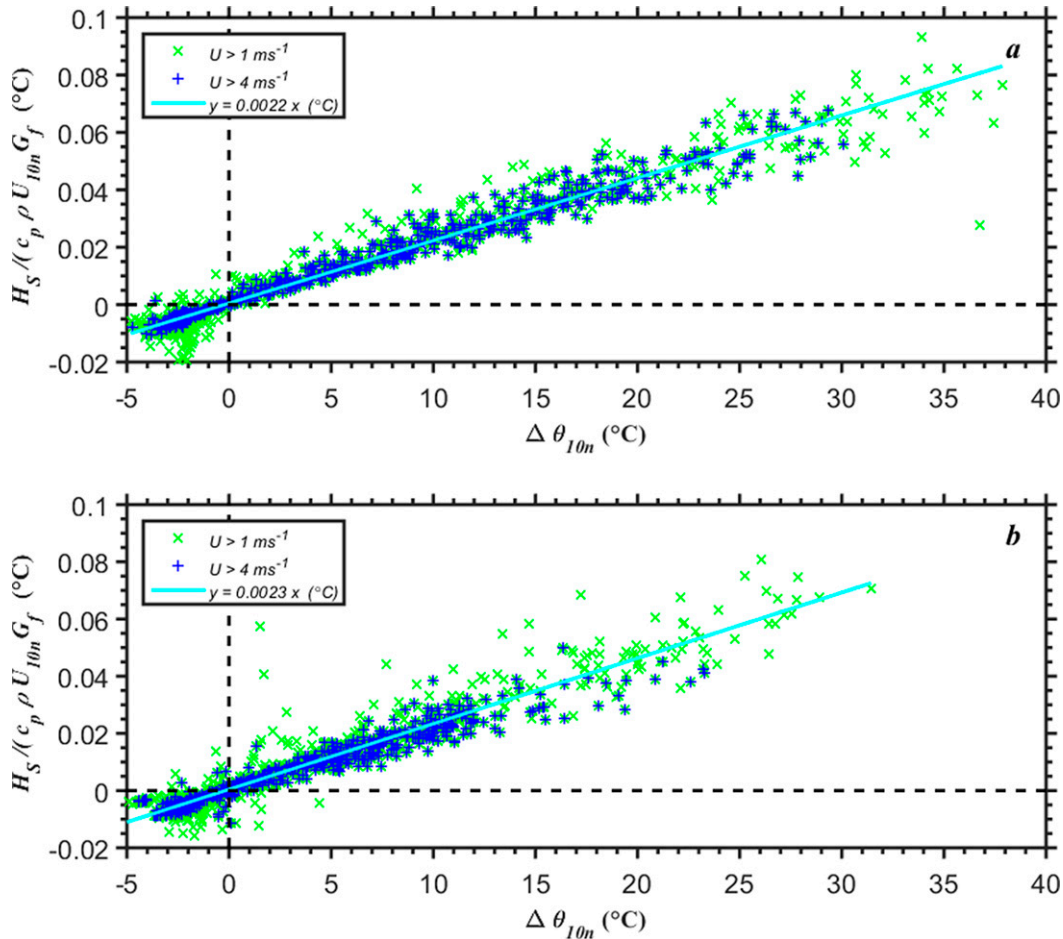


FIG. 7. Linear regression fit of half-hourly averaged covariance sensible heat flux normalized by  $c_p \rho U_{10m} G_f$  vs 10-m neutral surface air temperature difference for (a) the dry soil golden files (YD 240–270, 27 Aug–26 Sep 2016) and (b) the wet soil golden files period (YD 450–480, 25 Mar–24 Apr 2017). The green  $\times$  symbols are data for 10-m neutral wind speed greater than  $1 \text{ m s}^{-1}$ ; for blue  $+$  symbols only wind speed greater than  $4 \text{ m s}^{-1}$  are considered. The cyan solid lines are regressions based on the half-hourly averaged values for wind speed greater than  $1 \text{ m s}^{-1}$ .

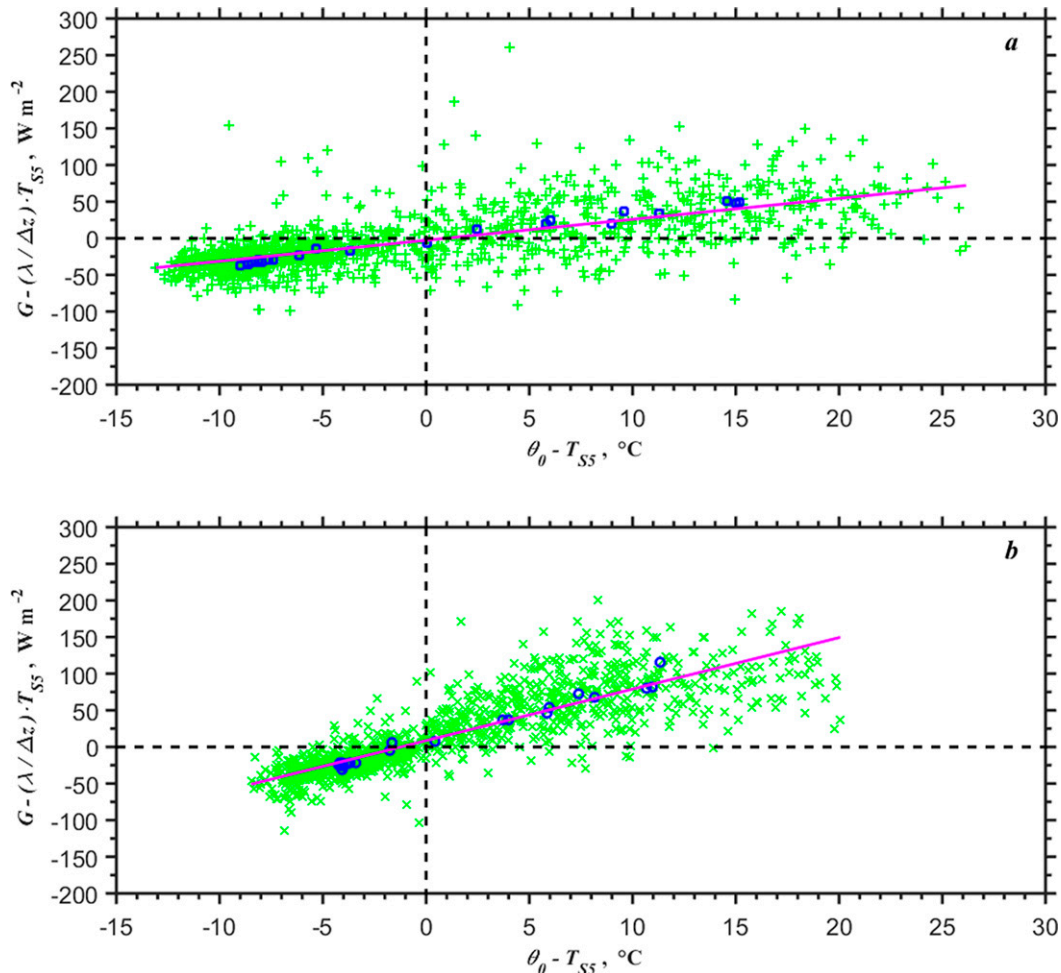


FIG. 8. The adjusted ground flux (residual) storage term vs temperature difference between surface ( $\theta_0$ ) and soil at 5-cm depth ( $T_{55}$ ) for (a) the dry soil golden files period (YD 240–270) and (b) the wet soil golden files period (YD 450–480). The green  $\times$  symbols are half-hourly averaged values; blue circles are derived from the mean diurnal cycle. The magenta solid lines are regressions with  $\lambda/\Delta z = 2.859 \text{ W m}^{-2} \text{ K}^{-1}$  for the dry soils and  $\lambda/\Delta z = 7.034 \text{ W m}^{-2} \text{ K}^{-1}$  for the wet soils based on the half-hourly averaged values.

2004; Cristea et al. 2013; Assouline et al. 2016; Cuxart and Boone 2020). In particular, the P-T parameter  $\alpha$  increases as the surface resistance to the evapotranspiration decreases; that is,  $\alpha$  increases with increasing the soil moisture (Cristea et al. 2013) and, according to De Bruin (1983),  $\alpha > 1$  for well-watered surfaces and  $\alpha < 1$  under dry conditions.

The value of  $f(e)$  in (11) varies from 0 to 1. According to Yao et al. [2015, Eq. (11)], the ecophysiological constraint function  $f(e)$  in (11) can be expressed as

$$f(e) = k_0 + k_1\theta_a + k_2\text{RH}^{\text{VPD}} + (k_3\text{NDVI} - k_4)\text{VPD}, \quad (12)$$

where VPD is the air vapor pressure deficit  $e_{\text{sat}}(\theta) - e$ , RH is the relative humidity (0 to 1), and NDVI the normalized difference vegetation index. The  $k_i$  ( $i = 0, \dots, 4$ ) are empirical coefficients given in Table 1 of Yao et al. (2015) for nine different surface types. We have chosen a type “GRA” (Yao

et al. 2015, their Table 1), which includes grassland and barren or sparsely vegetated soil (soil at the PS01 tower site is essentially a plowed fallow field with little vegetation).

To calculate  $H_L$  from a P-T type model, the soil heat flux  $G$  in (11) needs to be estimated. As mentioned earlier, we do not have direct measurements of the soil heat flux  $G$  at the WFIP2 Physics Site PS01. There are numerous approaches to compute the soil heat flux, that use different input data from in situ measurements (e.g., see Liebethal et al. 2005; Liebethal and Foken 2007; Gao et al. 2017b). Different methods for evaluating  $G$  can use various in situ measurements such as soil temperature, soil moisture, and net radiation. Furthermore, some parameterization approaches can be suitable for different times of the day. Here, we use measurements of soil temperature  $T_S(z)$  and soil moisture  $Q_S(z)$  to estimate  $G$  in (11) based on (6). Equation (6) can be now integrated for the interface down to some reference depth  $\Delta z$ . Near the surface we can linearly approximate  $G(z)$ , so

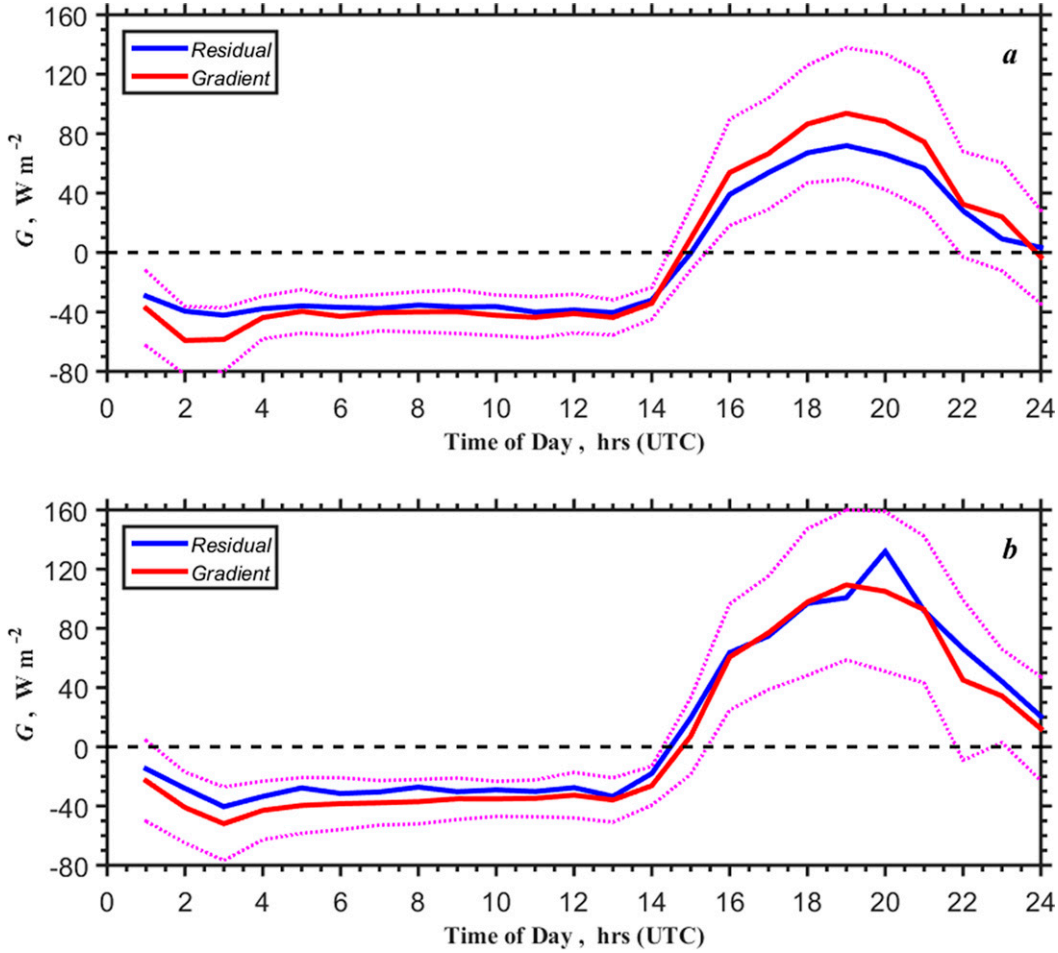


FIG. 9. Mean diurnal plot of ground flux  $G$  for (a) the dry soil golden files period (YD 240–270) and (b) the wet soil golden files period (YD 450–480). The blue lines are the residual estimate of  $G$  and the red lines are  $G$  computed via (15) based on the half-hourly averaged values. Magenta dotted lines show standard deviations for the gradient estimates of the ground flux in (15).

$$\int_0^z \left( G + z \frac{\partial G}{\partial z} \right) dz = G\Delta z + \frac{1}{2} \frac{\partial G}{\partial z} \Delta z^2 = \lambda [\theta_0 - T_S(\Delta z)]. \quad (13)$$

In this notation,  $G$  in (13) is the value at the interface  $z = 0$ , where also  $T_S(0) = \theta_0$  [cf. Eq. (8)]. The gradient term in (13) is estimated from the temporal change of the soil temperature

$$\rho_S c_{pS} \frac{\partial T_S}{\partial t} = - \frac{\partial G}{\partial z}, \quad (14)$$

where  $\rho_S$  is the soil density and  $c_{pS}$  is the soil specific heat. Thus,  $G$  can be estimated as the sum of a gradient and storage term (Garratt 1992):

$$G = \frac{\lambda}{\Delta z} [\theta_0 - T_S(\Delta z)] + \frac{1}{2} \rho_S c_{pS} \frac{\partial T_S}{\partial t} \Delta z. \quad (15)$$

The system of the hybrid bulk flux computations is summarized in Table 1. Execution of these requires specification of certain coefficients that we have determined by tuning to

agree with direct measurements at the PS01 site. Some other properties, such as  $\Delta_s$  and  $\gamma$  in Eq. (11), or atmospheric stability functions, are considered universal and we take them from the literature. For the turbulent fluxes, we need to determine the transfer coefficients  $C_H$  and  $C_D$ . Following the discussion in the appendix, we can estimate the 10-m neutral coefficients directly via

$$C_{X_{10m}} = \frac{\overline{w'x'}}{U_{10m} \Delta X_{10m} G_f}, \quad (16)$$

where  $x = u, \theta, \text{ or } q$ ,  $X = U, \theta, \text{ or } q$ , and  $\Delta X = X_0 - X_a$  is the difference between the surface value (zero for wind speed  $U$ ) and the value at reference height  $z$  in the atmosphere,  $G_f$  is the gustiness factor (see the appendix). Application of (16) is problematic when  $U_{10m}$  and/or  $\Delta X_{10m}$  are small. We can set minimum thresholds  $U_{th}$  and  $\Delta X_{th}$  for  $U_{10m}$  and  $\Delta X_{10m}$ , respectively, and average (16) for a subset of the data restricted to conditions where  $U_{10m} > U_{th}$  and  $|\Delta X_{10m}| > \Delta X_{th}$ . A variation on this approach is to do a linear regression of the form



$$\frac{\overline{w'x'}}{U_{10m}G_f} = a_x + b_x\Delta X_{10m}, \quad (17)$$

so that  $C_{X10m} = b_x$ . This has advantages for the heat flux because we do not have to restrict  $\Delta\theta_{10m}$  and the offset coefficient  $a_x$  in (17) gives an indication of relative bias between  $\theta_0$  and  $\theta_a$ . If there is no bias, the regression should pass through the origin; a temperature bias would be indicated as  $\delta X = -a_x/b_x$ . An example of half-hourly averaged covariance sensible heat flux normalized by  $c_p\rho U_{10m}G_f$  versus 10-m neutral surface–air temperature difference for the uninterrupted 30-day time series (golden files periods) is shown in Fig. 7 separately for dry soils (Fig. 7a) and for wet soils (Fig. 7b). In this case we examined fits where we have ignored observations with low wind speed (thresholds of  $U_{th} = 1$  and  $4 \text{ m s}^{-1}$  are used). These thresholds were selected based on a visual analysis of the data scatter in Fig. 7 and similar plots. The obvious outliers occur for winds less than  $4 \text{ m s}^{-1}$  but the fits yield about the same value for the Stanton number  $C_{H10m}$ , about  $2.20 \times 10^{-3}$  using (16) and  $2.15 \times 10^{-3}$  using (17) for dry soils (the uninterrupted 30-day time series, YD 240–270, 27 August–26 September 2016; see Figs. 3 and 4). For wet soils (the uninterrupted 30-day time series, YD 450–480, 25 March–24 April 2017; see Figs. 5 and 6), the corresponding values of  $C_{H10m}$  are  $2.30 \times 10^{-3}$  using (16) and  $2.39 \times 10^{-3}$  using (17). Similarly, results for the drag coefficient  $C_{D10m}$  are  $2.76 \times 10^{-3}$  (16) and  $2.29 \times 10^{-3}$  (17) for dry soil golden files (YD 240–270) and  $3.63 \times 10^{-3}$  (16) and  $3.21 \times 10^{-3}$  (17) for wet soil golden files (YD 450–480) for the thresholds of  $U_{th} = 1$  and  $4 \text{ m s}^{-1}$  (plots for  $C_{D10m}$  similar to Fig. 7 are not shown here). Note that the number of data points for the sensible heat measured during the dry soil golden files period (Fig. 7a) decreased to  $\approx 97\%$  of the original amount for wind speed greater than  $1 \text{ m s}^{-1}$  and  $\approx 59\%$  of the original amount for wind speed greater than  $4 \text{ m s}^{-1}$ , respectively. Similar values for the wet soil golden files period (Fig. 7b) were  $\approx 94\%$  and  $\approx 48\%$ , respectively.

A similar approach can be used to determine the ground flux; for Eq. (15) we do a linear regression of the form

$$G_{\text{res}} - \frac{1}{2}\rho_S c_{pS} \frac{\partial T_S}{\partial t} \Delta z = a_g + b_g[\theta_0 - T_S(\Delta z)], \quad (18)$$

so that  $\lambda/\Delta z = b_g$ . Because we do not have direct measurements of  $G$ , we have substituted the residual from an assumed energy balance:

$$G_{\text{res}} = R_{\text{net}} - H_S - H_L. \quad (19)$$

Thus, the residual term “Res” (all storage and transport contributions as well as other unspecified processes) in Eq. (7) is attributed in our model to the ground heat flux, that is, by  $G_{\text{res}} = G + \text{Res}$ . Based on this assumption, we apply a linear fit in Eq. (18) to calibrate the model. Note that Mauder et al. (2020, section 4) recently surveyed different methods when Res is attributed to  $H_S$  or  $H_L$  in order to close energy balance.

An example for the dry soil golden files period (YD 240–270) and the wet soil golden files period (YD 450–480) is shown in Fig. 8. Here we have plotted the individual half-hourly values (Fig. 8) and, to reduce the noise, values from the mean diurnal

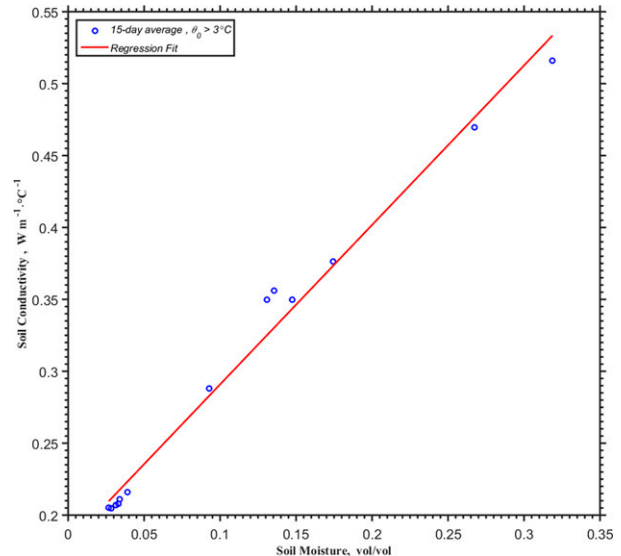


FIG. 10. Regression fit of the thermal conductivity of the soil  $\lambda$  vs soil moisture content at 5-cm depth  $Q_{S5}$ ; see Eq. (21) based on the data collected during the entire field campaign (311-day dataset from 24 Jun 2016 to 1 May 2017, YD 176–487).

cycle (Fig. 9). The fit yields a value of  $\lambda/\Delta z = 2.859$  and  $7.034 \text{ W m}^{-2} \text{ K}^{-1}$  for dry and wet soils, respectively. We have done these fits for 15-day increments throughout the entire experimental period (311-day dataset from 24 June 2016 to 1 May 2017, YD 176–487) and found that the thermal conductivity of the soil,  $\lambda$ , varies considerably but with a strong correlation to soil moisture (see discussion in appendix 4 of Garratt 1992). This correlation is illustrated in Fig. 10. Thus, based on the data presented in Fig. 10 for the entire field campaign, we estimate  $\lambda$  via

$$\lambda = 0.180 + 1.09Q_{S5}, \quad (20)$$

where  $Q_{S5}$  is the soil moisture measured at 5-cm depth. Of course, by tuning the coefficients to the residual flux, we are forcing our parameterization to, on average, produce a reasonable total energy balance.

We also examined the use of (11) and (12) to estimate the latent heat flux  $H_L$ . We chose coefficients appropriate for bare soil from Yao et al. (2015). However, we found that a constant value for the P-T coefficient  $\alpha$  gave poor results. So we adjusted  $\alpha$  in (11) to give a reasonable estimate of the mean flux and, as with the soil conductivity, we fit the values to soil moisture:

$$\alpha = 0.4 + 5Q_{S5}. \quad (21)$$

This is in good agreement with the values reported in literature for dry and well-watered surfaces (e.g., De Bruin 1983; Cristea et al. 2013; Assouline et al. 2016). Note, however, that Eq. (21) for the P-T parameter derived from the WFIP2 data is not a universal formula.

An example comparing direct covariance and bulk estimates of the sensible and latent heat fluxes for the dry and wet soil golden files is shown in Fig. 11. According to our half-hourly averaged data for the sensible heat flux  $H_S$ , the linear

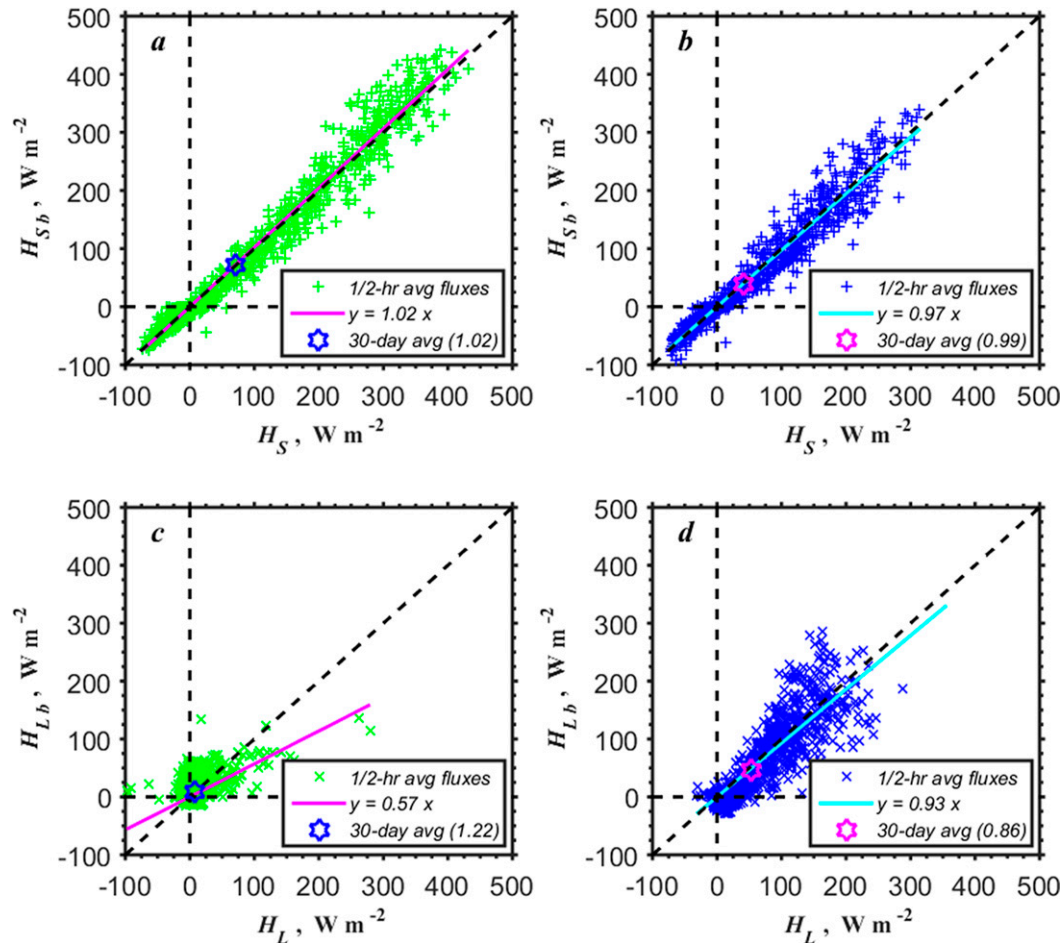


FIG. 11. Scatterplots of the bulk estimates of (a),(b) sensible heat flux  $H_S$  and (c),(d) latent heat flux  $H_L$  vs their measured (direct covariance) counterparts based on the half-hourly and monthly averaged data using (11) and (12) with  $\alpha = 0.4 + 5Q_{S5}$  ( $\alpha$  not to exceed 1.45). Plots in (a) and (c) represent the dry soil golden files (YD 240–270), and in (b) and (d) they represent the wet soil golden files period (YD 450–480). Correlation coefficients: (a)  $R^2 = 0.99$ , (b)  $R^2 = 0.98$ , (c)  $R^2 = 0.56$ , and (d)  $R^2 = 0.88$ .

regression forced through the origin is  $y = 1.02x$  with the correlation coefficient  $R^2 = 0.99$  in the case of the dry soil golden files (Fig. 11a) and the regression is  $y = 0.97x$  with  $R^2 = 0.98$  in the case of the wet soil golden files (Fig. 11b), respectively. Thus, on average, the scatterplots for  $H_S$  (Figs. 11a,b) show a fairly good agreement between direct covariance and bulk estimates. The scatter in the sensible heat flux is about what

we expect for covariance sampling error over half-hour averages (at least possible biases associated with the bulk flux algorithm are within the accuracy of the field turbulence data of  $\approx 20\%$ – $30\%$ , see Yaglom 1974). The scatter and bias between bulk and direct half-hour values of latent heat flux for the dry period (Fig. 11c) is considerably greater than that obtained for sensible heat flux but comparable to that for  $H_S$

TABLE 2. Summary of flux statistics (monthly averages indicated by angle brackets and standard deviations  $\sigma$ ) for the dry soil golden files (YD 240–270).

Flux variables	$\langle$ Bulk $\rangle$	$\langle$ Direct $\rangle$	$\sigma$ bulk	$\sigma$ direct
$G$ ( $\text{W m}^{-2}$ )	−2.4	—	58.9	—
$H_S$ ( $\text{W m}^{-2}$ )	71.5	69.9	131.2	126.9
$H_L$ ( $\text{W m}^{-2}$ )	9.0	7.4	20.0	22.3
$\tau$ ( $\text{N m}^{-1}$ )	0.10	0.12	0.11	0.13
$R_{\text{net}}$ ( $\text{W m}^{-2}$ )	—	72.8	—	173.0

TABLE 3. Summary of flux statistics (monthly averages indicated by angle brackets and standard deviations  $\sigma$ ) for the wet soil golden files (YD 450–480).

Flux variables	$\langle$ Bulk $\rangle$	$\langle$ Direct $\rangle$	$\sigma$ bulk	$\sigma$ direct
$G$ ( $\text{W m}^{-2}$ )	7.4	—	66.4	—
$H_S$ ( $\text{W m}^{-2}$ )	40.0	40.2	87.4	88.0
$H_L$ ( $\text{W m}^{-2}$ )	45.7	53.3	68.1	61.2
$\tau$ ( $\text{N m}^{-2}$ )	0.13	0.15	0.16	0.19
$R_{\text{net}}$ ( $\text{W m}^{-2}$ )	—	108.9	—	201.9

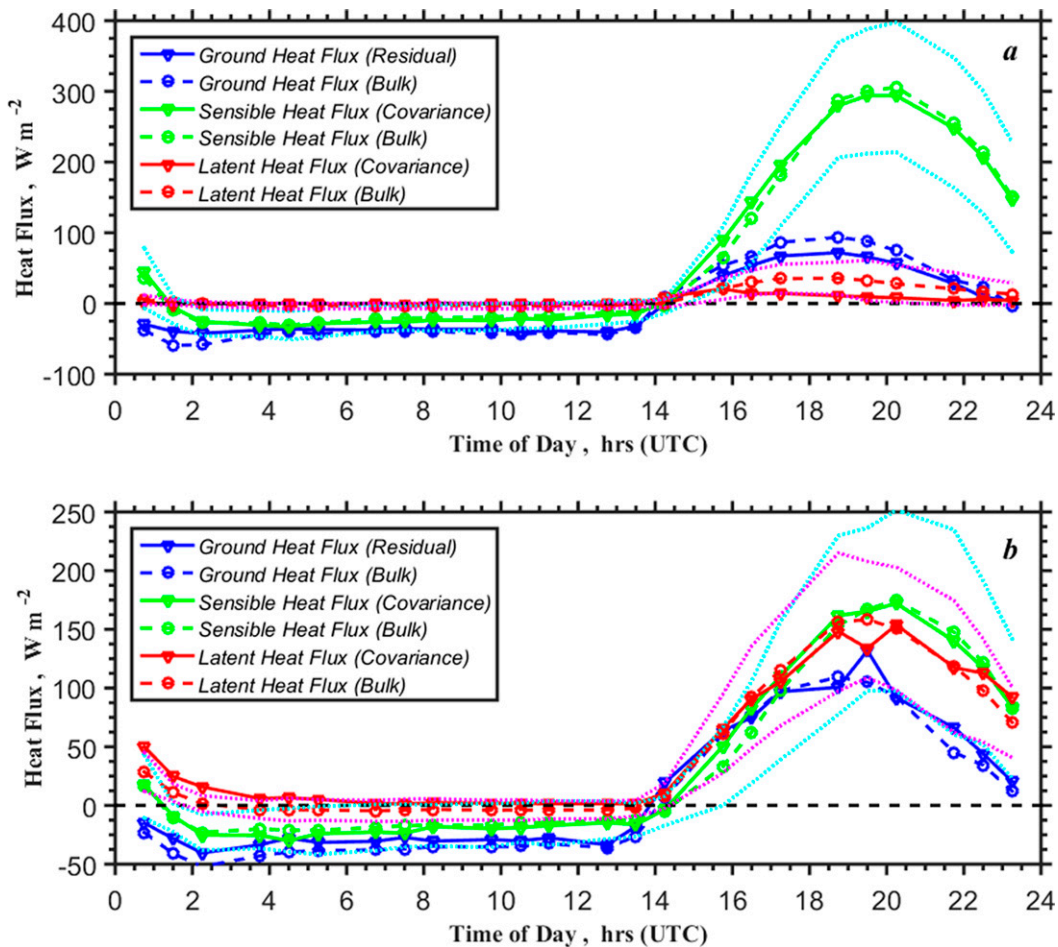


FIG. 12. Mean diurnal cycle of sensible, latent, and ground heat fluxes for (a) dry and (b) wet soil golden files periods. Direct measurements are solid lines with triangle symbols; the bulk estimates are dashed lines with circle symbols based on the half-hourly averaged values. Magenta and cyan dotted lines show standard deviations for the latent and sensible bulk heat fluxes, respectively.

for the wet period (Fig. 11d). According to our data, the linear regression forced through the origin is  $y = 0.57x$  with the correlation coefficient  $R^2 = 0.56$  in the case of the dry soil golden files (Fig. 11c) and the regression is  $y = 0.93x$  with  $R^2 = 0.88$  in the case of the wet soil golden files (Fig. 11d), respectively. The scatterplots of the measured turbulent fluxes versus their bulk counterparts (Fig. 11) can be considered as a validation test for our hybrid bulk flux algorithm.

One further point to consider is the nature of tuning coefficients in the context of imperfect observations. If we examine (9) we see one primary coefficient  $C_{H10n}$  and three observational variables  $S$ ,  $\theta_0$ , and  $\theta_a$ . In principle, we could tune the transfer coefficient to give the correct observed mean flux for some period. Alternatively, we could look for inconsistencies in the observables and perhaps apply a correction. It is clear that  $\theta_0$  is subject to significant error, on the order of  $1^\circ\text{C}$ , because it is computed from upward and downward radiative fluxes that are each uncertain by roughly  $5 \text{ W m}^{-2}$  [e.g., see specifications for Eppley

Precision Infrared Radiometer (PIR) pyrgeometer]. Also, note that both  $G$  and  $LW_{\text{up}}$  contain  $\theta_0$ , so adjusting  $\theta_0$  will affect their mean values. Another factor is that for time periods of a few weeks, the variance of each of the fluxes is dominated by the diurnal cycle. A summary of flux statistics (monthly mean and standard deviation) for the dry and wet soil golden files periods is given in Tables 2 and 3, respectively. Values in Tables 2 and 3 are based on the data presented in Fig. 11. So, if we take the mean diurnal cycle of one of the fluxes (e.g., Fig. 9), we can diagnose the relevant errors in transfer coefficients or conductivity versus biases in the observed temperatures. The strength of the diurnal cycle is principally proportional to  $C_{H10n}$  or  $\lambda$ . If the difference in the day–night excursions of the bulk fluxes matches the observed fluxes, then the coefficients are about right. Offsets in the mean diurnal cycles can be reduced by “correcting”  $\theta_0$ ,  $T_S$ , or  $\theta_a$ . For sensible heat, the slope from (17) yields the transfer coefficient that will match the diurnal cycle and the intercept indicates if there is a mismatch



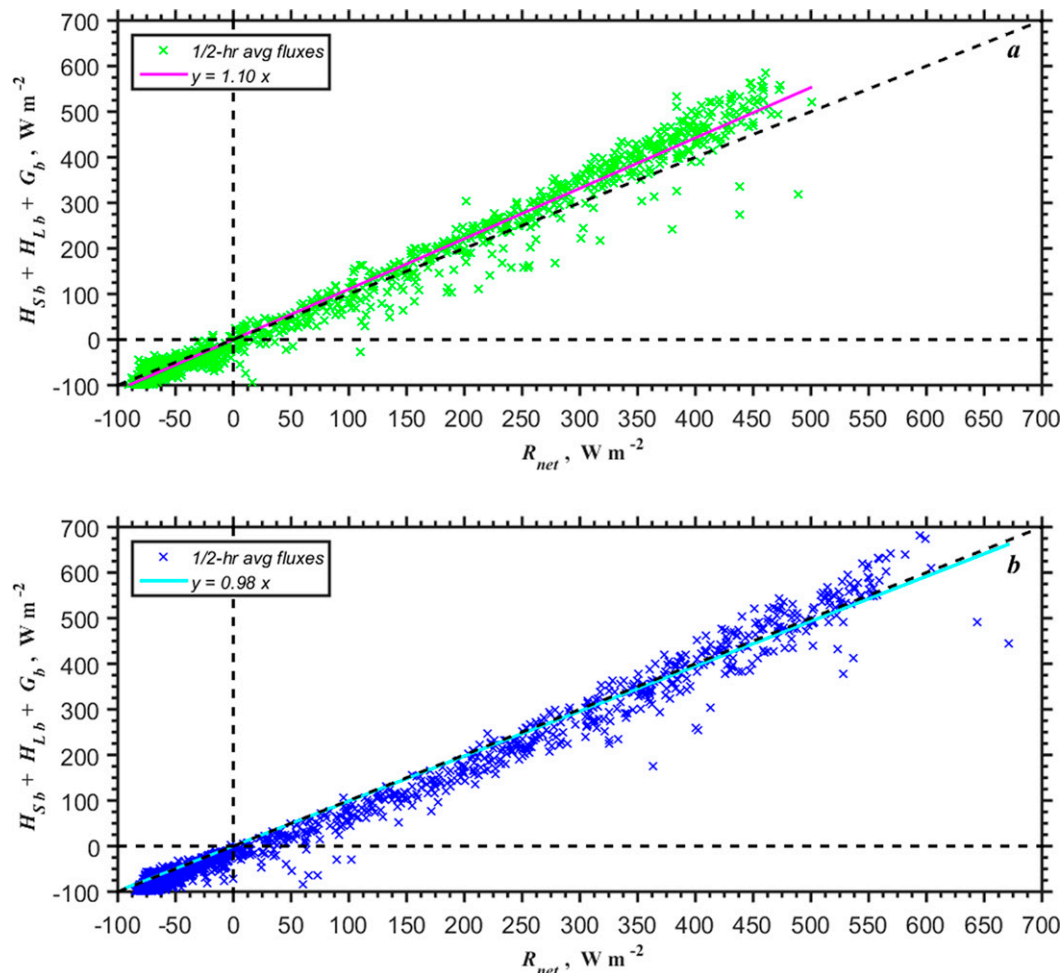


FIG. 13. Net surface energy balance from bulk flux calculations for (a) the dry soil golden files (YD 240–270) and (b) the wet soil golden files period (YD 450–480). Observed net radiation  $R_{net}$  vs the sum of the sensible, latent, and ground fluxes as yielded by (9), (11), and (15). Correlation coefficients: (a)  $R^2 = 0.99$  and (b)  $R^2 = 0.99$ .

between  $\theta_0$  and  $\theta_a$ . The small intercept bias in Fig. 7 gives an indication of relatively good correlation between the sensible heat flux  $H_S$  and  $\Delta\theta_{10m}$  under the assumption that  $\theta_0$  and  $\theta_a$  were accurately measured. Both Figs. 7 and 8 indicate reasonable compatibility of  $\theta_0$  and  $T_{SS}$ . Although in general, the bulk flux estimates provide reasonable renditions of the mean and standard deviation of the fluxes and the mean diurnal cycles (Fig. 12), the bulk estimates of the latent heat flux are somewhat higher than the measured ones during the daytime for dry soils (Fig. 12a). The sum of the three bulk fluxes yields a reasonable balance of the net radiation at half-hour time scales (Fig. 13). According to Fig. 13, the linear regression forced through the origin for the half-hourly data is  $y = 1.10x$  for the dry soil golden files and  $y = 0.98x$  for the wet soil golden files.

As mentioned earlier, direct measurements of the soil heat flux  $G$  with a heat flux plate were not available during the field campaign WFIP2. However, we use model estimates of  $G$  from the bulk flux algorithm described in this section to make estimates of the SEB closure in (4). Figure 14 shows the net surface

energy balance based on the measured sensible and latent heat fluxes  $H_S + H_L$  and bulk estimates of the ground heat flux  $G_b$  versus the net solar radiation  $R_{net}$ . Figures 14a and 14b show the incomplete energy balance equation,  $H_S + H_L$  versus  $R_{net}$ , whereas Figs. 14c and 14d are based on Eq. (4),  $H_S + H_L + G_b$  versus  $R_{net}$ . Plots in Figs. 14a and 14c represent the dry soil golden files (YD 240–270, 27 August–26 September 2016) and Figs. 14b and 14d represent the wet soil golden files period (YD 450–480, 25 March–24 April 2017). According to the data presented in Fig. 14, the SEB imbalance in the case of the incomplete energy balance equation, that is,  $H_S + H_L$  versus  $R_{net}$ , is about 20% for dry soils (Fig. 14a) and is about 27% for wet soils (Fig. 14b) for half-hourly averaged fluxes. However, including the bulk estimates of the ground heat flux  $G_b$  in the SEB closure equation, that is,  $H_S + H_L + G_b$  versus  $R_{net}$ , substantially reduces the SEB imbalance for each specific soil condition, (to about 5% in Fig. 14c, and 3% in Fig. 14d, respectively). The SEB imbalance is also reduced for 30-day-averaged data (cf. Figs. 14a,b and Figs. 14c,d, respectively). Note that plots of monthly means in Grachev et al.

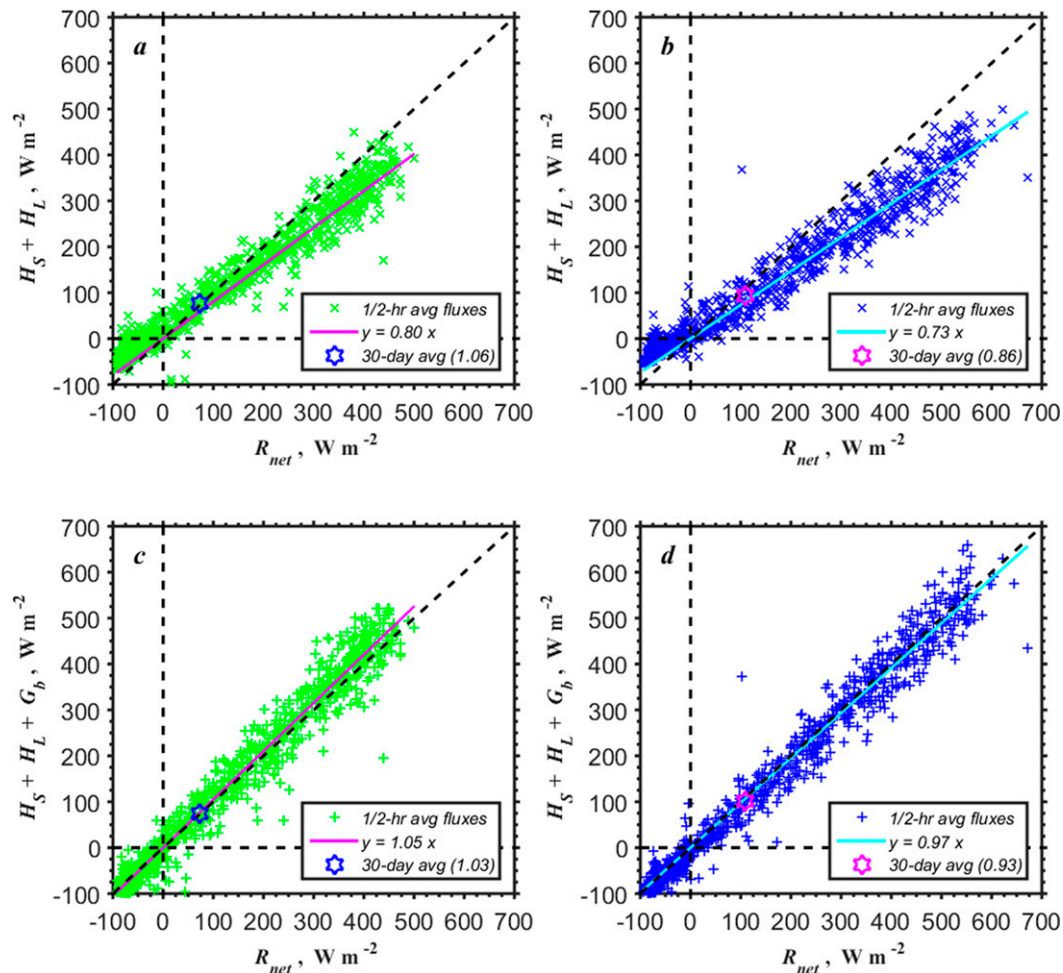


FIG. 14. Scatterplots of the net surface energy balance for (a),(b) the sum of the measured sensible and latent heat fluxes  $H_S + H_L$  and (c),(d) the sum of the measured  $H_S + H_L$  and bulk estimates of the ground heat flux  $G_b$  vs the net solar radiation  $R_{net}$  based on the half-hourly and monthly averaged data. Plots in (a) and (c) represent the dry soil golden files (YD 240–270), and in (b) and (d) they represent the wet soil golden files period (YD 450–480).

(2020, Fig. 13) (triangular symbols for dry and wet soils) and in Fig. 14 (blue and pink six-pointed star symbols) are based on the data presented in Tables 2 and 3.

Although the entire 311-day experimental period (YD 176–487) is used for regression fit of the soil thermal conductivity soil in Fig. 10, the model is calibrated based on the data collected during two 30-day golden files time periods separately for dry (YD 240–270) and wet (YD 450–480) soils (Figs. 3–6). At the same time, the golden files periods are used for model verification (Figs. 11–14) what may not look quite correct. Therefore, for the independent model verification we tested our model beyond the calibration periods (the golden files periods). We have selected two additional 15-day test periods for dry (YD 270–285) and wet (YD 435–450) soil conditions and then apply the model without further tuning. The choice of these time intervals associated with the availability of uninterrupted time series of relatively good data (see Grachev et al. 2020, Figs. 4–6). The results are shown in

Figs. 15 and 16 and, as expected, they did not change significantly as compared to the calibration golden files periods (cf. linear regressions and correlation coefficients for pairs Figs. 15–11 and Figs. 16–13).

## 5. Summary and discussion

While progress has been made in studying and in parameterizations turbulent fluxes of momentum, heat, and water vapor over horizontally homogeneous surfaces such as open ocean (Fairall et al. 1996, 2003) and sea ice or snow-covered surfaces (e.g., Andreas et al. 2010a,b), an equivalent level of progress in the development of simple bulk algorithms over land is not practical because of the complexity of the surface. Here we examine a land case that is just one step more complex than a water surface—relatively flat land with low vegetation. The parameterization of the turbulent fluxes for terrestrial sites and their representation in numerical models

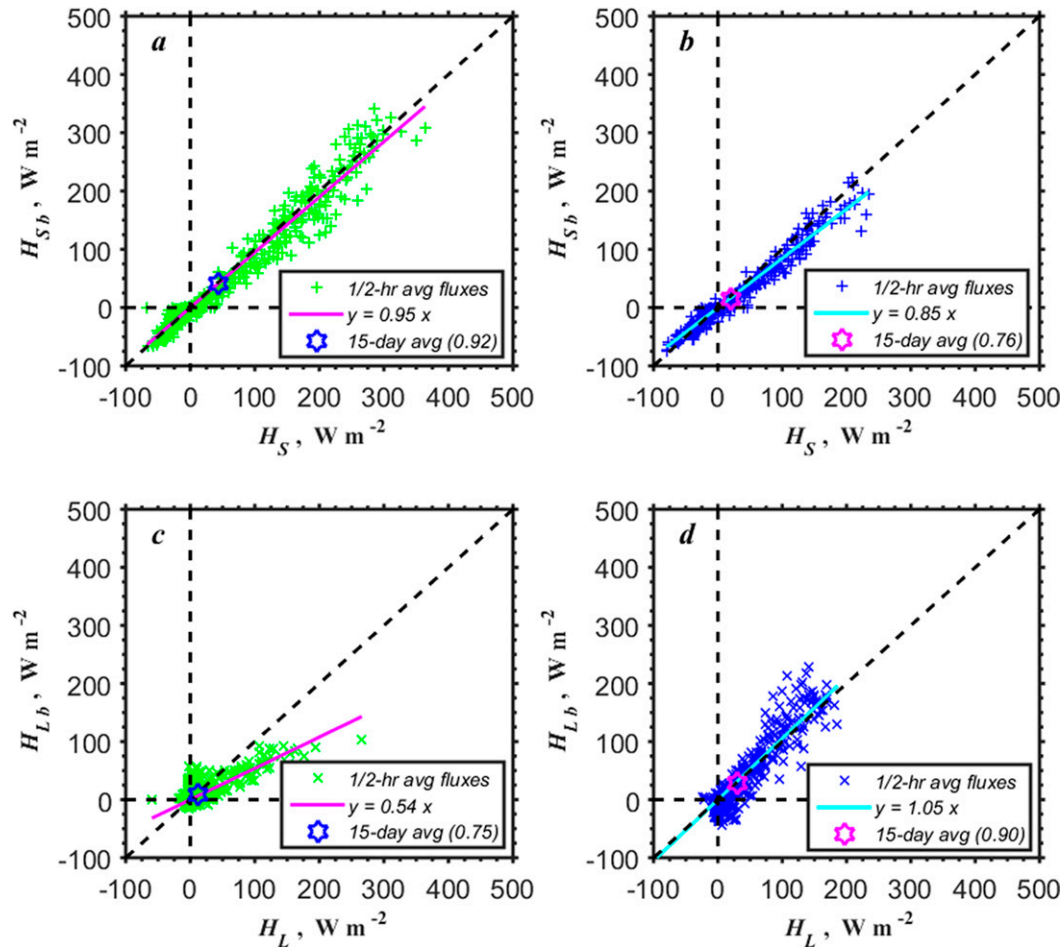


FIG. 15. As Fig. 11, but for (a),(c) YD 270–285 (dry soils) and (b),(d) YD 435–450 (wet soils). Correlation coefficients: (a)  $R^2 = 0.98$ , (b)  $R^2 = 0.98$ , (c)  $R^2 = 0.79$ , and (d)  $R^2 = 0.92$ .

is a challenging problem because of the spatial complexity of the underlying surface especially in the case of heterogeneous or patched terrain (e.g., when bare and vegetated surfaces coexist) or for nonsaturated conditions, which are common in arid and semiarid climates, and in complex terrain (e.g., Bou-Zeid et al. 2020; Cuxart and Boone 2020). Myriad different types of climates, soils, and vegetation add extra complexity in the problem. Another issue of the flux estimates from routine meteorological measurements over land is associated with the availability of the relevant model input parameters and their related uncertainties. This implies a need to use nontraditional synthetic methods and to work in an interdisciplinary framework.

Using the data from the second WFIP2 field campaign collected in the Columbia River Gorge area of irregular terrain near Wasco during 2016–17, we have developed and tested an optimized hybrid bulk flux algorithm for predicting the turbulent surface fluxes of momentum, sensible, and latent heat in (1)–(3) over dry and wet bare or lightly vegetated soil surfaces. The bulk flux algorithm combines (i) the traditional COARE bulk flux algorithm (Fairall et al. 1996, 2003)

adopted for overland situations for estimation of the turbulent fluxes of momentum  $\tau$  and the sensible heat  $H_S$  (section 3 and as described in the appendix), and (ii) a modified P-T model in (11) with physically based ecophysiological constraints in (12) by Yao et al. (2015) to estimate the latent heat flux  $H_L$  (or moisture flux) (section 4). Whereas bulk estimates of  $\tau$  and  $H_S$  are derived from a traditional approach, which is based on the transfer coefficients (drag coefficient and Stanton number), aerodynamic and scalar roughness lengths, and MOST flux–profile relationships, modeled values of  $H_S$  are evaluated from a modified P-T approach, which is essentially based on the SEB in Eq. (4) (i.e., on the conservation of energy principle). Note also, that a MOST-based flux–profile approach or a bulk flux algorithm requires measurements of the relevant variables (e.g., wind speed and  $T/RH$ ) at two different levels whereas a SEB-type model needs data (e.g., radiative fluxes) from a single level only. One may classify this approach as a hybrid or synthetic (composite) approach because it uses different physical principles for parameterization of the turbulent fluxes. Our hybrid bulk flux approach is summarized in Table 1.



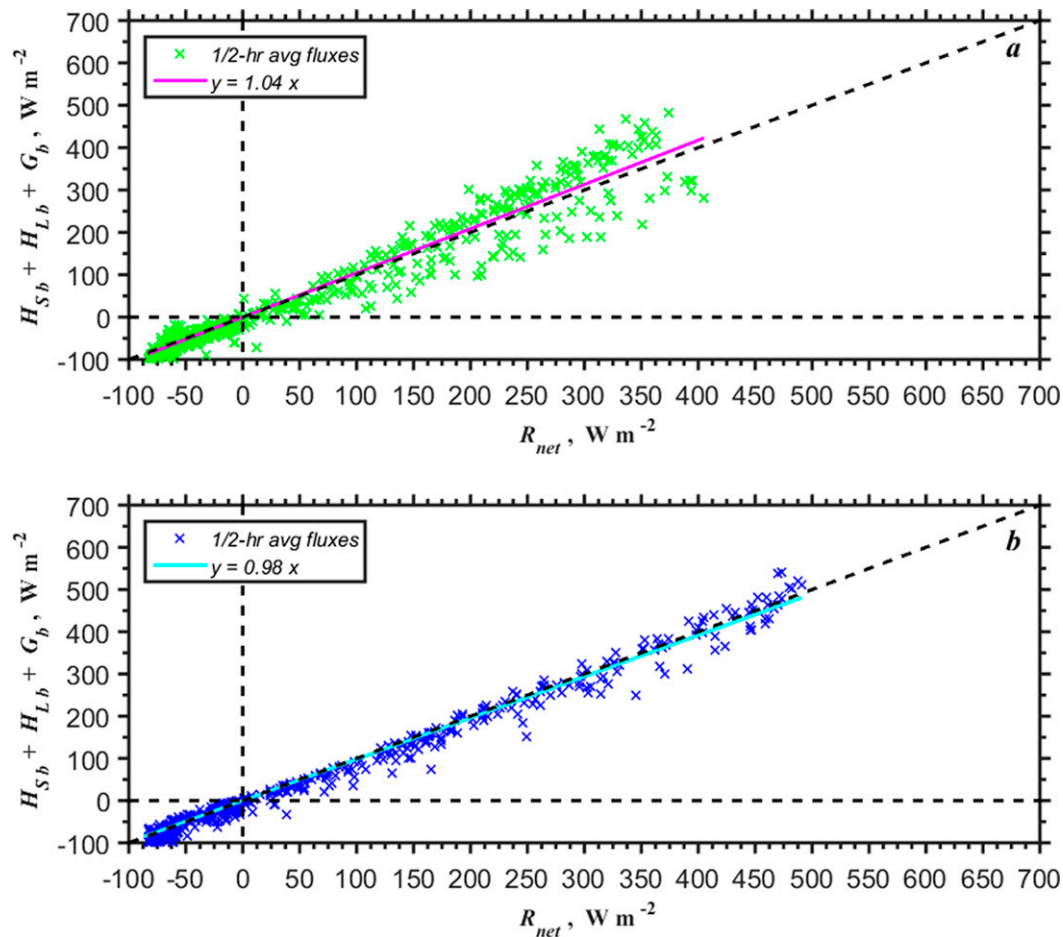


FIG. 16. As in Fig. 13, but for (a) YD 270–285 (dry soils) and (b) YD 435–450 (wet soils). Correlation coefficients: (a)  $R^2 = 0.97$  and (b)  $R^2 = 0.99$ .

Thus, the novelty in our bulk flux algorithm for a terrestrial tower site is associated with the use of a hybrid approach to predict the turbulent fluxes, when even the turbulent energy fluxes  $H_S$  and  $H_L$  are estimated from two completely different physical principles. As mentioned above, a two-level aerodynamic method for a turbulent flow in the case of  $\tau$  and  $H_S$  estimates (i.e., a traditional bulk approach) and the first law of thermodynamics at the interface for  $H_L$  estimates (one may say that these two approaches are “apples and oranges”). In addition, a hybrid approach is characterized by flexible logic. For example,  $H_L$  can be estimated from another model based on the SEB in Eq. (4), whereas  $\tau$  and  $H_S$  can be derived from a gradient method (requiring meteorological measurements at two atmospheric levels) rather a traditional bulk approach (requiring meteorological measurements at one atmospheric level and estimation of  $\theta_0$ ,  $z_{0x}$  at the surface–atmosphere interface, see section 4). Obviously, other options for the flux estimates are also possible in the framework of a hybrid approach (e.g., see Basu 2019 for discussion).

In this study, we use two 30-day-long uninterrupted time series of the data separately for dry and wet soil conditions

(WFIP2 golden files). Time periods from 27 August to 26 September 2016 (YD 240–270) and 25 March to 24 April 2017 (YD 450–480 with respect to 1 January 2016) were selected to calibrate and verify parameterizations for the surface fluxes over dry and wet soil surfaces, respectively (see Grachev et al. 2020 for further detail). We sorted the data into dry and wet categories based on the soil temperature and soil moisture measured at 5-cm depth (section 2). The direct measurements of the surface fluxes (turbulent and radiative) and other ancillary atmospheric/soil parameters made during WFIP2 for different soil conditions (dry and wet) are used to optimize and tune the hybrid bulk algorithm. In particular, our results suggest that the P-T coefficient  $\alpha$  varies with soil moisture according to (21). Because direct measurements of the soil heat flux  $G$  (e.g., with a heat flux plate) were not available during the field campaign WFIP2,  $G$  in the P-T model (11) was estimated from the Fourier’s law of heat conduction in (6) based measurements of soil temperature and soil moisture. Dependence of the thermal conductivity of the soil  $\lambda$  in (6) versus soil moisture content at 5-cm depth for the entire field campaign (Fig. 10) was estimated via Eq. (21).

The bulk flux estimates have been validated against the eddy-covariance fluxes (Fig. 11). According to linear regression slopes for the scatterplots shown in Fig. 11, the bulk flux estimates for  $H_S$  and  $H_L$  predicted by the hybrid bulk flux algorithm provide reasonable agreement on average (within a few percent except  $H_L$  for the dry period) with the measured half-hourly averaged flux values (see also Tables 2 and 3). In this study we also discuss the SEB closure over dry and wet surfaces at various time scales (from half-hourly to monthly averages) based on the modeled and measured fluxes for the dry and wet soil golden files periods (Figs. 13 and 14). In addition, we tested the model beyond the 30-day golden files calibration periods without further tuning (Figs. 15 and 16). The bulk flux algorithm described in section 4 is optimized for the data collected at the WFIP2 Physics Site PS01. However, our model and its modifications can be used for other similar flux-tower sites and similar field campaigns.

It can be assumed that our approach is applicable to other similar sites in which advection, heterogeneity, etc. are considered not to be relevant. This is because our approach is based on the first principles; that is, on the aerodynamic method for a turbulent mixing in the case of  $\tau$  and  $H_S$  estimates and the first law of thermodynamics at the interface for  $H_L$  estimates. To apply our approach to other locations, the tunable model parameters associated with surface properties and soil type (e.g.,  $z_0$  and  $\lambda$ ) must be changed. However, it is necessary to keep in mind that our approach as well as other land surface models and remote sensing applications assume a closed energy balance only for four main terms in (4), allowing to compute explicitly missing terms as the residual of the others (e.g., Cuxart et al. 2015; Mauder et al. 2020, and references therein). The limitation of this approach is associated with neglecting of all storage and transport contributions, and other unspecified processes. This can lead to systematic bias in estimates of the energy fluxes (in our case  $H_L$ ). Mauder et al. (2020) recently survey different methods of estimating the magnitude of the SEB residual imbalance, which can improve the predictability of the energy fluxes.

*Acknowledgments.* This work was supported by the National Oceanic and Atmospheric Administration (NOAA) Atmospheric Science for Renewable Energy (ASRE) program and by the U.S. Department of Energy (DoE) DE-EE0007605 interagency agreement that supports DoE FOA DE-FOA-0000984. The University of Notre Dame team was supported by DOE-WFIP2-SUB-001. HJSF was also supported by NSF Grants AGS-1565535 and 1921554.

## APPENDIX

### Turbulent Bulk Flux Algorithm

In a traditional bulk turbulent flux algorithm in Eqs. (8)–(10), we make a distinction between the scalar-averaged wind speed (i.e., the mean wind speed)  $S$  and the vector-averaged wind speed (i.e., the magnitude of the mean wind vector)  $U$  at reference height  $z$  [for discussion see Grachev et al. (1998), section 3.1, and Akylas et al. (2003), section 2a].

The vector averaging of the wind speed first takes the average of the longitudinal and lateral wind speed components,  $u$  and  $v$ , respectively, and then takes the square,

$$U = (\bar{u}^2 + \bar{v}^2)^{1/2}, \quad (\text{A1})$$

whereas the scalar averaging first takes the square and then average

$$S = (\bar{u}^2 + \bar{v}^2)^{1/2}. \quad (\text{A2})$$

Combining (A1) and (A2) with the definition of variance leads to a relationship between  $U$  and  $S$ :

$$S^2 - U^2 = (\bar{u}^2 - \bar{u}^2) + (\bar{v}^2 - \bar{v}^2) = \sigma_u^2 + \sigma_v^2, \quad (\text{A3})$$

where  $\sigma_u$  and  $\sigma_v$  are the horizontal velocity variances. Relationship (A3) is also known as the gustiness assumption (e.g., Fairall et al. 1996; Grachev et al. 1998). According to (A3),  $S$  in such conditions is the vector sum  $U$  and the convective gustiness velocity,  $U_G = (\sigma_u^2 + \sigma_v^2)^{1/2}$ :

$$S^2 = U^2 + U_G^2 = U G_f^2, \quad (\text{A4})$$

where  $G_f = S/U$  is called the gustiness factor. In convective conditions, large-scale circulations embracing the entire convective boundary layer (CBL) create random gusts that crucially affect the surface fluxes. In the COARE bulk algorithm, for unstable stratification  $U_G = \beta w_*$  where  $\beta \approx 1.25$  (Fairall et al. 1996) and  $w_* = (\overline{w'\theta_v}gh/\theta_v)^{1/3}$  is the Deardorff (1970) convective velocity scale ( $\theta_v$  is the virtual temperature, and  $h$  is the CBL height). A key point of (A4) is employment of  $\sigma_u, \sigma_v \sim w_*$  (Panofsky et al. 1977); that is, a convective gust is proportional to the Deardorff (1970) velocity scale  $w_*$ , which is added to the mean wind speed  $U$ . Thus, under light wind conditions (in the free-convection limit)  $U \rightarrow 0$  whereas  $S \rightarrow w_*$ . Note that variances of the horizontal wind components in the convective surface layer are practically independent of height and, therefore, do not follow the traditional surface-layer scaling.

It is obvious that vector or scalar averaging can be applied to the turbulent stress as well since the instantaneous vector of the wind stress has the same direction as the wind vector (Grachev et al. 1998; Akylas et al. 2003). Similar to  $S$  defined by Eqs. (A2)–(A4), the scalar averaged stress  $\tau_s$  has a finite limit as  $U$  approaches zero. In this case, random CBL-scale coherent structures produce a local log profile in the layer attached to the bottom of the large eddies. This local velocity profile generates a local stress (the “minimum friction velocity”). Thus, the concept of gustiness immediately leads to a “minimum friction velocity” assumption (e.g., Businger 1973; Schumann 1988; Sykes et al. 1993; Akylas et al. 2003) also referred as the convection-induced stress regime (Grachev et al. 1997, 1998; Zilitinkevich et al. 1998, 2005, 2006). In fact, free convection can be considered as a particular case of forced convection.

Zilitinkevich et al. (1998, 2005, 2006) developed a more detailed theoretical model for the nonlocal momentum and heat transfer. The vector or scalar averaging of the turbulent stress is related in particular to the time averaging procedure. Mahrt et al. (1996) reported a substantial difference of the drag coefficient in light winds for different averaging times and vector/scalar wind speed averaging procedures. According to Mahrt et al. (1996), higher values of the drag coefficient occur for a 10-min time-averaging period compared to 60-min averaged values. The vector averaging of the surface stress would be appropriate for determination of the average, net large scale force acting on a surface (e.g., for description of the surface currents for measurements over sea surface). Note that both the COARE and SHEBA bulk flux algorithms as well as Eq. (8) are based on the vector averaging of the turbulent stress when  $\tau = \rho u_*^2 \propto SU$ , whereas the scalar averaged wind stress assumes  $\tau_S = \rho u_s^2 \propto S^2$  (where  $u_{*s}$  is the friction velocity based on the scalar averaging).

The COARE bulk flux algorithm is described in detail by Fairall et al. (1996, 2003) but it is sketched here. The transfer coefficients in (8)–(10) are partitioned into individual profile components [Fairall et al. 1996, Eq. (5)]:

$$C_D = c_d^{1/2} c_d^{1/2}, \quad C_H = c_d^{1/2} c_h^{1/2}, \quad C_E = c_d^{1/2} c_e^{1/2} \quad (\text{A5})$$

The bulk variables are used to compute so-called Monin–Obukhov (MO) scaling parameters [Fairall et al. 1996, Eq. (9)]:

$$u_*^2 = C_D S U, \quad \theta_* = -c_h^{1/2} \Delta\theta, \quad q_* = -c_e^{1/2} \Delta q. \quad (\text{A6})$$

Traditionally, the transfer coefficients (A6) are adjusted to neutral conditions using MO similarity theory via [e.g., Fairall et al. 1996, Eq. (6)]

$$c_d^{1/2} = \frac{c_{dn}^{1/2}}{1 - \frac{c_{dn}^{1/2}}{\kappa} \Psi_m(\zeta)}, \quad c_h^{1/2} = \frac{c_{hn}^{1/2}}{1 - \frac{c_{hn}^{1/2}}{\kappa} \Psi_h(\zeta)},$$

$$c_e^{1/2} = \frac{c_{en}^{1/2}}{1 - \frac{c_{en}^{1/2}}{\kappa} \Psi_h(\zeta)}. \quad (\text{A7})$$

Here,  $\Psi_m(\zeta)$  and  $\Psi_h(\zeta)$  are the MO profile functions for mean profiles of wind speed and scalars in the surface layer,  $\kappa \approx 0.4$  is the von Kármán constant. In neutral conditions ( $\zeta \equiv 0$ ) the  $\Psi$  functions obey  $\Psi_m(\zeta) = \Psi_h(\zeta) = 0$ . Subscript  $n$  in  $c_{dn}$ ,  $c_{hn}$ , and  $c_{en}$  in (A7) denotes the value in neutral conditions. The MO stability parameter  $\zeta = z/L$  ( $L$  is the Obukhov length) is defined by

$$\zeta = \frac{\kappa g z}{\theta_a} \frac{\theta_v}{u_*^2}. \quad (\text{A8})$$

Here,  $g$  is the acceleration due to gravity and, historically, the von Kármán constant is included in the definition of  $L$  and  $\zeta$  simply by convention. Subscript  $v$  in  $\theta_v$  in (A8)

denotes the virtual temperature. The neutral transfer coefficients in (A7) are uniquely related to the aerodynamic,  $z_0$ , and scalar,  $z_{0\theta}$  and  $z_{0q}$ , roughness lengths through

$$c_{dn}^{1/2} = \frac{\kappa}{\log z/z_0}, \quad c_{hn}^{1/2} = \frac{\kappa}{\log z/z_{0\theta}}, \quad c_{en}^{1/2} = \frac{\kappa}{\log z/z_{0q}}. \quad (\text{A9})$$

The transfer coefficients depend on height via (A9), but the roughness lengths are fixed for a given surface. Traditionally the transfer coefficients for operational or practical considerations are also represented at a standard reference height of 10 m and neutral conditions and denoted as  $C_{D10m}$ ,  $C_{H10m}$ , and  $C_{E10m}$ . These 10-m neutral transfer coefficients are computed from  $U_{10m}$ ,  $\Delta\theta_{10m}$  and  $\Delta q_{10m}$  [see Fairall et al. 2003, Eqs. (31) and (32)].

## REFERENCES

- Akylas, E., Y. Tsakos, M. Tombrou, and D. P. Lalas, 2003: Considerations on minimum friction velocity. *Quart. J. Roy. Meteor. Soc.*, **129**, 1929–1943, <https://doi.org/10.1256/qj.01.73>.
- Andreas, E. L., T. W. Horst, A. A. Grachev, P. O. G. Persson, C. W. Fairall, P. S. Guest, and R. E. Jordan, 2010a: Parameterizing turbulent exchange over summer sea ice and the marginal ice zone. *Quart. J. Roy. Meteor. Soc.*, **136**, 927–943, <https://doi.org/10.1002/qj.618>.
- , P. O. G. Persson, R. E. Jordan, T. W. Horst, P. S. Guest, A. A. Grachev, and C. W. Fairall, 2010b: Parameterizing turbulent exchange over sea ice in winter. *J. Hydrometeorol.*, **11**, 87–104, <https://doi.org/10.1175/2009JHM1102.1>.
- Assouline, S., D. Li, S. Tyler, J. Tanny, S. Cohen, E. Bou-Zeid, M. Parlange, and G. G. Katul, 2016: On the variability of the Priestley–Taylor coefficient over water bodies. *Water Resour. Res.*, **52**, 150–163, <https://doi.org/10.1002/2015WR017504>.
- Bariteau, L., D. Helmig, C. W. Fairall, J. E. Hare, J. Hueber, and E. K. Lang, 2010: Determination of oceanic ozone deposition by ship-borne eddy covariance flux measurements. *Atmos. Meas. Tech.*, **3**, 441–455, <https://doi.org/10.5194/amt-3-441-2010>.
- Basu, S., 2019: Hybrid profile-gradient approaches for the estimation of surface fluxes. *Bound.-Layer Meteorol.*, **170**, 29–44, <https://doi.org/10.1007/s10546-018-0391-1>.
- Bianco, L., and Coauthors, 2019: Impact of model improvements on 80-m wind speeds during the second Wind Forecast Improvement Project (WFIP2). *Geosci. Model Dev.*, **12**, 4803–4821, <https://doi.org/10.5194/gmd-12-4803-2019>.
- Blomquist, B. W., B. J. Huebert, C. W. Fairall, L. Bariteau, J. B. Edson, J. E. Hare, and W. R. McGillis, 2014: Advances in air–sea CO<sub>2</sub> flux measurement by eddy correlation. *Bound.-Layer Meteorol.*, **152**, 245–276, <https://doi.org/10.1007/s10546-014-9926-2>.
- Bou-Zeid, E., W. Anderson, G. G. Katul, and L. Mahrt, 2020: The persistent challenge of surface heterogeneity in boundary-layer meteorology: A review. *Bound.-Layer Meteorol.*, **177**, 227–245, <https://doi.org/10.1007/s10546-020-00551-8>.
- Businger, J. A., 1973: A note on free convection. *Bound.-Layer Meteorol.*, **4**, 323–326, <https://doi.org/10.1007/BF02265241>.
- Cava, D., D. Contini, A. Donato, and P. Martano, 2008: Analysis of short-term closure of the surface energy balance above



- short vegetation. *Agric. For. Meteor.*, **148**, 82–93, <https://doi.org/10.1016/j.agrformet.2007.09.003>.
- Cristea, N. C., S. K. Kampf, and S. J. Burges, 2013: Revised coefficients for Priestley–Taylor and Makkink–Hansen equations for estimating daily reference evapotranspiration. *J. Hydrol. Eng.*, **18**, 1289–1300, [https://doi.org/10.1061/\(ASCE\)HE.1943-5584.0000679](https://doi.org/10.1061/(ASCE)HE.1943-5584.0000679).
- Cuxart, J., and A. A. Boone, 2020: Evapotranspiration over land from a boundary-layer meteorology perspective. *Bound.-Layer Meteor.*, **177**, 427–459, <https://doi.org/10.1007/s10546-020-00550-9>.
- , L. Conangla, and M. A. Jiménez, 2015: Evaluation of the surface energy budget equation with experimental data and the ECMWF model in the Ebro Valley. *J. Geophys. Res. Atmos.*, **120**, 1008–1022, <https://doi.org/10.1002/2014JD022296>.
- Deardorff, J. W., 1970: Convective velocity and temperature scales for the unstable planetary boundary layer and for Rayleigh convection. *J. Atmos. Sci.*, **27**, 1211–1213, [https://doi.org/10.1175/1520-0469\(1970\)027<1211:CVATSF>2.0.CO;2](https://doi.org/10.1175/1520-0469(1970)027<1211:CVATSF>2.0.CO;2).
- De Bruin, H. A. R., 1983: A model for the Priestley–Taylor parameter  $\alpha$ . *J. Climate Appl. Meteor.*, **22**, 572–578, [https://doi.org/10.1175/1520-0450\(1983\)022<0572:AMFTPT>2.0.CO;2](https://doi.org/10.1175/1520-0450(1983)022<0572:AMFTPT>2.0.CO;2).
- , and A. A. M. Holtslag, 1982: A simple parameterization of the surface fluxes of sensible and latent heat during daytime compared with the Penman–Monteith concept. *J. Appl. Meteor.*, **21**, 1610–1621, [https://doi.org/10.1175/1520-0450\(1982\)021<1610:ASPOTS>2.0.CO;2](https://doi.org/10.1175/1520-0450(1982)021<1610:ASPOTS>2.0.CO;2).
- Fairall, C. W., E. F. Bradley, D. P. Rogers, J. B. Edson, and G. S. Young, 1996: Bulk parameterization of air–sea fluxes for Tropical Ocean–Global Atmosphere Coupled–Ocean Atmosphere Response Experiment. *J. Geophys. Res.*, **101**, 3747–3764, <https://doi.org/10.1029/95JC03205>.
- , —, J. E. Hare, A. A. Grachev, and J. B. Edson, 2003: Bulk parameterization of air–sea fluxes: Updates and verification for the COARE algorithm. *J. Climate*, **16**, 571–591, [https://doi.org/10.1175/1520-0442\(2003\)016<0571:BPOASF>2.0.CO;2](https://doi.org/10.1175/1520-0442(2003)016<0571:BPOASF>2.0.CO;2).
- Fisher, J. B., K. P. Tu, and D. D. Baldocchi, 2008: Global estimates of the land–atmosphere water flux based on monthly AVHRR and ISLSCP-II data, validated at 16 FLUXNET sites. *Remote Sens. Environ.*, **112**, 901–919, <https://doi.org/10.1016/j.rse.2007.06.025>.
- Foken, T., 2008: The energy balance closure problem: An overview. *Ecol. Appl.*, **18**, 1351–1367, <https://doi.org/10.1890/06-0922.1>.
- , 2017: *Micrometeorology*. 2nd ed. Springer, 362 pp., <https://doi.org/10.1007/978-3-642-25440-6>.
- , F. Wimmer, M. Mauder, C. Thomas, and C. Liebenthal, 2006: Some aspects of the energy balance closure problem. *Atmos. Chem. Phys.*, **6**, 4395–4402, <https://doi.org/10.5194/acp-6-4395-2006>.
- Gao, Z., H. Liu, G. G. Katul, and T. Foken, 2017a: Non-closure of the surface energy balance explained by phase difference between vertical velocity and scalars of large atmospheric eddies. *Environ. Res. Lett.*, **12**, 034025, <https://doi.org/10.1088/1748-9326/aa625b>.
- , and Coauthors, 2017b: A novel approach to evaluate soil heat flux calculation: An analytical review of nine methods. *J. Geophys. Res. Atmos.*, **122**, 6934–6949, <https://doi.org/10.1002/2017JD027160>.
- Garratt, J. R., 1992: *The Atmospheric Boundary Layer*. Cambridge University Press, 316 pp.
- Grachev, A. A., C. W. Fairall, and S. S. Zilitinkevich, 1997: Surface-layer scaling for the convection-induced stress regime. *Bound.-Layer Meteor.*, **83**, 423–439, <https://doi.org/10.1023/A:1000281625985>.
- , —, and S. E. Larsen, 1998: On the determination of the neutral drag coefficient in the convective boundary layer. *Bound.-Layer Meteor.*, **86**, 257–278, <https://doi.org/10.1023/A:1000617300732>.
- , L. Bariteau, C. W. Fairall, J. E. Hare, D. Helmig, J. Hueber, and E. K. Lang, 2011: Turbulent fluxes and transfer of trace gases from ship-based measurements during TexAQS 2006. *J. Geophys. Res.*, **116**, D13110, <https://doi.org/10.1029/2010JD015502>.
- , E. L. Andreas, C. W. Fairall, P. S. Guest, and P. O. G. Persson, 2015: Similarity theory based on the Dougherty–Ozmidov length scale. *Quart. J. Roy. Meteor. Soc.*, **141**, 1845–1856, <https://doi.org/10.1002/qj.2488>.
- , C. W. Fairall, B. W. Blomquist, H. J. S. Fernando, L. S. Leo, S. F. Otárola-Bustos, J. M. Wilczak, and K. L. McCaffrey, 2020: On the surface energy balance closure at different temporal scales. *Agric. For. Meteor.*, **281**, 107823, <https://doi.org/10.1016/j.agrformet.2019.107823>.
- Hao, Y., J. Baik, and M. Choi, 2019: Developing a soil water index-based Priestley–Taylor algorithm for estimating evapotranspiration over East Asia and Australia. *Agric. For. Meteor.*, **279**, 107760, <https://doi.org/10.1016/j.agrformet.2019.107760>.
- Higgins, C. W., 2012: A-posteriori analysis of surface energy budget closure to determine missed energy pathways. *Geophys. Res. Lett.*, **39**, L19403, <https://doi.org/10.1029/2012GL052918>.
- Jacobs, A. F. G., B. G. Heusinkveld, and A. A. M. Holtslag, 2008: Towards closing the surface energy budget of a mid-latitude grassland. *Bound.-Layer Meteor.*, **126**, 125–136, <https://doi.org/10.1007/s10546-007-9209-2>.
- Kondo, J., N. Saigusa, and T. Sato, 1990: A parameterization of evaporation from bare soil surfaces. *J. Appl. Meteor.*, **29**, 385–389, [https://doi.org/10.1175/1520-0450\(1990\)029<0385:APOEFB>2.0.CO;2](https://doi.org/10.1175/1520-0450(1990)029<0385:APOEFB>2.0.CO;2).
- Kustas, W. P., C. S. T. Daughtry, and P. J. Van Oevelen, 1993: Analytical treatment of the relationship between soil heat flux/net radiation ratio and vegetation indices. *Remote Sens. Environ.*, **46**, 319–330, [https://doi.org/10.1016/0034-4257\(93\)90052-Y](https://doi.org/10.1016/0034-4257(93)90052-Y).
- , J. M. Norman, T. J. Schmugge, and M. C. Anderson, 2004: Mapping surface energy fluxes with radiometric temperature. *Thermal Remote Sensing in Land Surface Processes*, D. A. Quattrochi and J. C. Luvall, Eds., CRC Press, 205–253.
- Leuning, R., E. van Gorsel, W. J. Massman, and P. R. Isaac, 2012: Reflections on the surface energy imbalance problem. *Agric. For. Meteor.*, **156**, 65–74, <https://doi.org/10.1016/j.agrformet.2011.12.002>.
- Lhomme, J. A., 1997: A theoretical basis for the Priestley–Taylor coefficient. *Bound.-Layer Meteor.*, **82**, 179–191, <https://doi.org/10.1023/A:1000281114105>.
- Li, Z. L., R. L. Tang, Z. M. Wan, Y. Y. Bi, C. H. Zhou, B. H. Tang, G. J. Yan, and X. Y. Zhang, 2009: A review of current methodologies for regional evapotranspiration estimation from remotely sensed data. *Sensors*, **9**, 3801–3853, <https://doi.org/10.3390/s90503801>.
- Liebenthal, C., and T. Foken, 2007: Evaluation of six parameterization approaches for the ground heat flux. *Theor. Appl. Climatol.*, **88**, 43–56, <https://doi.org/10.1007/s00704-005-0234-0>.

- , B. Huwe, and T. Foken, 2005: Sensitivity analysis for two ground heat flux calculation approaches. *Agric. For. Meteor.*, **132**, 253–262, <https://doi.org/10.1016/j.agrformet.2005.08.001>.
- Mahrt, L., D. Vickers, J. Howell, J. Højstrup, J. M. Wilczak, J. Edson, and J. Hare, 1996: Sea surface drag coefficients in the Risø Air Sea Experiment. *J. Geophys. Res.*, **101**, 14327–14335, <https://doi.org/10.1029/96JC00748>.
- Majazi, N. P., C. M. Mannaerts, A. Ramoelo, R. Mathieu, A. Nickless, and W. Verhoef, 2017: Analysing surface energy balance closure and partitioning over a semi-arid savanna FLUXNET site in Skukuza, Kruger National Park, South Africa. *Hydrol. Earth Syst. Sci.*, **21**, 3401–3415, <https://doi.org/10.5194/hess-21-3401-2017>.
- Masseroni, D., C. Corbari, and M. Mancini, 2014: Limitations and improvements of the energy balance closure with reference to experimental data measured over a maize field. *Atmosfera*, **27**, 335–352, [https://doi.org/10.1016/S0187-6236\(14\)70033-5](https://doi.org/10.1016/S0187-6236(14)70033-5).
- Mauder, M., and Coauthors, 2007: The energy balance experiment EBEX-2000. Part II: Intercomparison of eddy-covariance sensors and post-field data processing methods. *Bound.-Layer Meteor.*, **123**, 29–54, <https://doi.org/10.1007/s10546-006-9139-4>.
- , T. Foken, and J. Cuxart, 2020: Surface-energy-balance closure over land: A review. *Bound.-Layer Meteor.*, **177**, 395–426, <https://doi.org/10.1007/s10546-020-00529-6>.
- Meyers, T. P., and S. E. Hollinger, 2004: An assessment of storage terms in the surface energy balance of maize and soybean. *Agric. For. Meteor.*, **125**, 105–115, <https://doi.org/10.1016/j.agrformet.2004.03.001>.
- Monteith, J. L., 1965: Evaporation and environment in the state and movement of water in living organism. *Proceedings of the Society for Experimental Biology*, Cambridge University Press, 205–234.
- Olson, J. B., and Coauthors, 2019: Improving wind energy forecasting through numerical weather prediction model development. *Bull. Amer. Meteor. Soc.*, **100**, 2201–2220, <https://doi.org/10.1175/BAMS-D-18-0040.1>.
- Oncley, S. P., and Coauthors, 2007: The energy balance experiment EBEX-2000. Part I: Overview and energy balance. *Bound.-Layer Meteor.*, **123**, 1–28, <https://doi.org/10.1007/s10546-007-9161-1>.
- Panofsky, H. A., H. Tennekes, D. A. Lenschow, and J. C. Wyngaard, 1977: The characteristics of turbulent velocity components in the surface layer under convective conditions. *Bound.-Layer Meteor.*, **11**, 355–361, <https://doi.org/10.1007/BF02186086>.
- Penman, H. L., 1948: Natural evaporation from open water, bare soil and grass. *Proc. Roy. Soc. London*, **193A**, 120–145, <https://doi.org/10.1098/rspa.1948.0037>.
- Pereira, A. R., 2004: The Priestley–Taylor parameter and the decoupling factor for estimating reference evapotranspiration. *Agric. For. Meteor.*, **125**, 305–313, <https://doi.org/10.1016/j.agrformet.2004.04.002>.
- Priestley, C., and R. Taylor, 1972: On the assessment of surface heat flux and evaporation using large-scale parameters. *Mon. Wea. Rev.*, **100**, 81–92, [https://doi.org/10.1175/1520-0493\(1972\)100<0081:OTAOSH>2.3.CO;2](https://doi.org/10.1175/1520-0493(1972)100<0081:OTAOSH>2.3.CO;2).
- Schumann, U., 1988: Minimum friction velocity and heat transfer in the rough surface layer of a convective boundary layer. *Bound.-Layer Meteor.*, **44**, 311–326, <https://doi.org/10.1007/BF00123019>.
- Shaw, W., and Coauthors, 2019: The second Wind Forecast Improvement Project (WFIP2): General overview. *Bull. Amer. Meteor. Soc.*, **100**, 1687–1699, <https://doi.org/10.1175/BAMS-D-18-0036.1>.
- Stoy, P. C., and Coauthors, 2013: A data-driven analysis of energy balance closure across FLUXNET research sites: The role of landscape scale heterogeneity. *Agric. For. Meteor.*, **171–172**, 137–152, <https://doi.org/10.1016/j.agrformet.2012.11.004>.
- Su, Z., 2002: The Surface Energy Balance System (SEBS) for estimation of turbulent heat fluxes. *Hydrol. Earth Syst. Sci.*, **6**, 85–100, <https://doi.org/10.5194/hess-6-85-2002>.
- Sykes, R. I., D. S. Henn, and W. S. Lewellen, 1993: Surface-layer description under free-convection conditions. *Quart. J. Roy. Meteor. Soc.*, **119**, 409–421, <https://doi.org/10.1002/qj.49711951103>.
- Venturini, V., L. Rodriguez, and G. Bisht, 2011: Comparison among different modified Priestley and Taylor equations to calculate actual evapotranspiration with MODIS data. *Int. J. Remote Sens.*, **32**, 1319–1338, <https://doi.org/10.1080/01431160903547965>.
- Wilczak, J. M., S. P. Oncley, and S. A. Stage, 2001: Sonic anemometer tilt correction algorithms. *Bound.-Layer Meteor.*, **99**, 127–150, <https://doi.org/10.1023/A:1018966204465>.
- , and Coauthors, 2019: The second Wind Forecast Improvement Project (WFIP2): Observational field campaign. *Bull. Amer. Meteor. Soc.*, **100**, 1701–1723, <https://doi.org/10.1175/BAMS-D-18-0035.1>.
- Wilson, K., and Coauthors, 2002: Energy balance closure at FLUXNET sites. *Agric. For. Meteor.*, **113**, 223–243, [https://doi.org/10.1016/S0168-1923\(02\)00109-0](https://doi.org/10.1016/S0168-1923(02)00109-0).
- Yaglom, A. M., 1974: Data on turbulence characteristics in the atmospheric surface layer. *Izv. Akad. Sci. USSR*, **10**, 341–352.
- Yao, Y., and Coauthors, 2013: MODIS-driven estimation of terrestrial latent heat flux in China based on a modified Priestley–Taylor algorithm. *Agric. For. Meteor.*, **171–172**, 187–202, <https://doi.org/10.1016/j.agrformet.2012.11.016>.
- , and Coauthors, 2014: Validation and application of the modified satellite-based Priestley–Taylor algorithm for mapping terrestrial evapotranspiration. *Remote Sens.*, **6**, 880–904, <https://doi.org/10.3390/rs6010880>.
- , and Coauthors, 2015: A satellite-based hybrid algorithm to determine the Priestley–Taylor parameter for global terrestrial latent heat flux estimation across multiple biomes. *Remote Sens. Environ.*, **165**, 216–233, <https://doi.org/10.1016/j.rse.2015.05.013>.
- Zilitinkevich, S. S., A. A. Grachev, and J. C. R. Hunt, 1998: Surface frictional and non-local heat/mass transfer in the shear-free convective boundary layer. *Buoyant Convection in Geophysical Flows*, E. J. Plate et al., Eds., NATO ASI Series, Vol. 513, Kluwer, 83–113, [https://doi.org/10.1007/978-94-011-5058-3\\_4](https://doi.org/10.1007/978-94-011-5058-3_4).
- , and Coauthors, 2005: The effect of large eddies on the convective heat/mass transfer over complex terrain: Advanced theory and its validation against experimental and les data. *Croat. Meteor. J.*, **40**, 20–26.
- , and Coauthors, 2006: The influence of large convective eddies on the surface layer turbulence. *Quart. J. Roy. Meteor. Soc.*, **132**, 1423–1456, <https://doi.org/10.1256/qj.05.79>.